Pore-Scale Network Modeling of Microporosity in Low-Resistivity Pay Zones of Carbonates

By
© 2019
Nijat Hakimov
B.Sc., Azerbaijan State Oil Academy, 2013

Submitted to the graduate degree program in Chemical and Petroleum Engineering and the Graduate Faculty of the University of Kansas in partial fulfillment of the requirements
for the degree of Master of Science.

Chair: Dr. Amirmasoud Kalantari-Dahaghi

Dr. Shahin Negahban

Dr. Arsalan Zolfaghari

Date Defended: 3rd of June, 2019

The thesis committee for Nijat Hakimov certifies that this is
the approved version of the following thesis:

Pore-Scale Network Modeling of Microporosity in Low-Resistivity Pay Zones of Carbonates

Chair: Dr. Amirmasoud Kalantari-Dahaghi

Date Approved: 3rd of June, 2019

Abstract

Carbonates present an important research area as classical empirical methods primarily developed for sandstone characterizations give erroneous results when being applied to carbonates. Specifically, the question of applicability of the Archie equation for these rocks is of great interest in the industry since it is directly related to reserves estimation. Archie equation often calculates high water saturation for intervals dominated by carbonates which would yield zero or little water-cut when being put on production. This phenomenon is known as “Low Resistivity Pay” (LRP). The problem arises from the inherent multi-scale heterogeneity of these rock types where different scales of pore populations constitute the pore space. As a result, the traditional techniques employed in digital rock physics has to be modified for accurate descriptions of the pore space in carbonates. Here in this work, we develop a state-of-the-art pore-scale network model (PSNM) that populates pore space for the microporous zones of carbonates and consequently, simulates displacement sequences during drainage and imbibition. To generate representative pore networks, the digital 3D images of the pore space should be larger than the representative elementary volume (REV) of the sample where all the effective pore space (i.e., contributing to the flow) are fully resolved. Existence of mixed-wet states in carbonates reduces the minimum pore sizes that contribute to the flow of the wetting phase. At the same time, inherent heterogeneity of carbonates increases their REV. This means that high-resolution images of large sample volumes have to be collected and processed. This, however, is not possible due to the physical and computational power limitations of the current imaging tools and computers. Therefore, it is often the case that the 3D image of a REV does not have high enough resolution, thus,

overlooking a large number of micropores, which usually account for a significant portion of the pore space in carbonates.

In this work, we develop a PSNM to investigate microporosity impact on the electrical and transport properties of 2D (lattice-based) and 3D pore networks. We have addressed the resolution problem by generating stochastic pore networks spatially located within the domains of unresolved zones (i.e., microporosity). The model stochastically reconstructs the pore space at higher resolutions based on the given input parameters of local porosity and pore size distribution for the microporous zones. We use two carbonate samples: one outcrop of Estaillades limestone and one reservoir limestone. The latter is taken from the Mississippian formation of the Osagean age in the STACK play in Oklahoma. For this interval, traditional techniques suggest high water saturation, however, core analysis reveals a significant oil saturation throughout the zone.

The results indicate a strong effect of the pore size distribution on the electrical and transport properties of these carbonate samples. The model allows to simulate and explain non-Archie behavior of the Resistivity Index curve. It also allows investigating the extent to which microporosity can have an impact on the petrophysical properties of carbonates by identifying key parameters with the biggest impact on the simulated properties.

Acknowledgments

First of all, I would like to express my deepest appreciation to my graduate advisor Dr. Amirmasoud Kalantari-Dahaghi for giving me this opportunity to join his research team back in Fall 2017 and for his support and help during my research project. Also, I would like to extend my deepest gratitude to one of the most hard-working people I have ever met — Dr. Arsalan Zolfaghari — for helping me numerous times to overcome very tough obstacles during my research and for being to me as a brother and as a friend at the times when I needed support. I appreciate the constant help that he has offered me even outside academia. Besides, I am very grateful to Prof. Shahin Negahban for his helpful comments on my project and I sincerely appreciate the time he took to hold frequent meetings with me to share his expertise in the field of my research.

Also, I am very thankful to Gary Gunter from Schlumberger and Geoff Vice from Fairway Resources for their useful feedback on my research project. I also would like to thank Prof. Paul Willhite for supervising me during my first semester at KU when I was working as a TA for his class.

Also, I would like to extend my sincere thanks to Martha Kehr at the CPE department for her help and support during all these years at KU. I am also grateful to all of my co-workers and friends and all the kind people that I met here and which supported me and helped me during this long journey.

And last, but not least, as for everything in life, I'm always thankful to my parents and to my brother for their endless support, love, and belief in me.

Table of Contents

List of Figures

List of Tables

Chapter 1. Introduction and problem statement

The first chapter introduces the main tools and concepts that have been used in this work. Particularly, first of all, we discuss the importance of the research on carbonates and the challenges associated with them. We specifically consider two major problems that the researchers encounter while dealing with carbonates in two different areas. Secondly, we discuss the common cause of these problems — microporosity — and review the general pore space characterization methods commonly used in Digital Rock Physics to address these problems. Finally, we specifically focus on the technique used in this work called Pore-Network Modelling (PNM) and present the ideas and the assumptions it is based on.

Experts estimate that carbonate reservoirs hold more than 60% of the world's oil reserves and 40% of the world's gas reserves (Ahmed 2010, Al-Marzouqi et al. 2010, Sheng 2013). Especially, for the Middle East region, the statistics get even more drastic with carbonate formations accounting for 70% of oil and 90% of gas reserves (Gundogar et al. 2016). These numbers spotlight the strategic importance of carbonate reservoirs in the context of future energy supply. Therefore, it is of great significance to accurately characterize carbonates, especially, considering the extremely complex nature of these formations.

Generally, porous media characterization has always been a major area of research in different fields, such as petroleum engineering, hydrology, and environmental and biological sciences. Various studies have shown the linkage between small scale events at the pore level and their corresponding large scale effect at the core level. Over the past few years, a lot of attention has been attracted to develop models for the simulation of

different pore-scale events. With the recent development of supercomputers and imaging technologies, our understanding of different pore-level physics has been improved. However, there are still unaddressed challenges, particularly, with respect to some of the commonly used hypotheses and scale-up issues.

From the modeling point of view, the first important step is to obtain a representative pore space structure for the medium of interest. This can be done by various imaging techniques, using different modalities (Xiong et al., 2016), or other methods such as, Mercury Intrusion Porosimetry (MIP) (Leon y Leon, 1998) and Gas Adsorption (Thommes et al., 2006). Non-imaging techniques can provide little details about the complex topology of the pore space. They are primarily limited to extraction of pore size distribution with the assumption that injected fluid has access to all and every pore and throat. Imaging techniques, on the other hand, can be used to characterize topological properties of a sample for each individual pore and throat as long as resolution allows. These techniques include X-ray computed micro-tomography (micro-CT), scanning electron microscopy (SEM) with Focused Ion Beams (FIB). Maximum resolution of SEM alone can vary in the range of 1-20 nm, while FIB can go lower down to less than 1 nm. Combination of these two techniques allows achieving voxel dimensions of tens of nanometers (Xiong et al., 2016). However, FIB/SEM is destructive imaging method, while micro-CT imaging techniques are non-destructive and non-invasive, and they are the most commonly used technique to create representative 3D images of porous media. Imaging time can vary up to several hours depending on the resolution for the commercially available CT-scanners in the market (Table 1.1). However, synchrotron CT-scanner can do the same within minutes due to higher X-ray flux (Xiong et al., 2016).

CT scanner	Spatial resolution
Medical	200-500 µm
Industrial	2-100 µm
Synchrotron	1-50 µm

Table 1.1. Micro-CT scanner resolutions (Xiong et al., 2016).

Having 3D images of the pore space, researchers have developed two inherently different methods to simulate multiphase fluid flow at pore levels, i.e., (1) direct numerical models and (2) network models (Bultreys et al., 2016) (Table 1.2).

<table>
<tr><th colspan="2">Image-based Porous Media reconstruction Models</th></tr>
<tr><td>Pore Network Models (PNM):</td><td rowspan="6">Direct Model (Direct pore space structure without modification)</td></tr>
<tr><td>Statistical reconstruction (from 2D images)</td></tr>
<tr><td>Regular network model (for example, cubic lattice)</td></tr>
<tr><td>Direct mapping models:
• Medial axis
• Maximum ball</td></tr>
<tr><td>Grain-based model (geological process-based reconstruction)</td></tr>
<tr><td>Two-scale PNM (for heterogeneous rocks)</td></tr>
<tr><th colspan="2">Corresponding Pore-Scale Flow Models</th></tr>
<tr><td>Quasi-static multi-phase flow model (capillary dominated flow)</td><td>Lattice-Boltzmann</td></tr>
<tr><td>Dynamic multi-phase flow model (viscosity and gravity effect considered)</td><td>Computational Fluid Dynamics</td></tr>
<tr><td rowspan="4"></td><td>Other particle methods:</td></tr>
<tr><td>Smoothed Particle</td></tr>
<tr><td>Moving particle semi-implicit model</td></tr>
<tr><td>Molecular dynamics and Monte Carlo</td></tr>
<tr><td></td><td>Direct Hydrodynamics method</td></tr>
</table>

Table 1.2. Summary of the existing pore-scale flow simulation models.

Direct models use pore space images ‘directly’ (or real pore geometry from images) to simulate fluid flow. This group of models includes methods such as Lattice-Boltzmann (Pan et al, 2004, Boek et al, 2010, Ramstad et. al, 2010), Computational Fluid Dynamics

(CFD) (Raeini et al., 2015, Icardi et al., 2014), and Inscribed Sphere Movement (Mohammadmoradi et al., 2017). These models are computationally expensive and instable (Meakin et al., 2009). They are mostly developed for 2D images, single phase flow, and has not reached to the level to reliably predict relative permeability and capillary pressures even in more homogenous systems. It is interesting to note that not many researchers have tried to simulate multiphase flow using direct methods. Raeini et al. (2015) tried to study capillary trapping impact by solving full Navier-Stokes equations for two-phase flow on micro-CT images of Berea sandstone and LV60 sandpack. They compared the results to the experiment and to quasi-static Pore-Network Modeling (PNM) simulation. They showed a better match for the direct simulation results with that of the experiments. Their PNM simulations had significant deviation from the experimental results. Direct simulation results matched the experiment, while PNM simulation predicted higher residual non-wetting phase saturation for water injection in the direction reverse to primary drainage, especially for LV60 sandpack. However, it is worth to mention that viscosity and density for both fluids were to set to that of water at room temperature.

LBM has been successfully used for single flow simulations, however, multiphase flow simulation involves a lot of challenges, due to numerical instability it becomes problematic to implement it for multiphase flow of fluids with large density and viscosity ratios (for example, water-gas systems) (Meakin et al., 2009, Chin et. al, 2002).

Not many researchers have tried to simulate multiphase flow directly on pore-scale images. The early works were done on two-dimensional models without comparison to experimental data (Pan et. al, 2004). Boek et al. (2010) conducted Latice-Boltzmann simulations for single-phase flow on 2D micro-model of Berea and for two-phase flow on

3D model of Bentheimer. However, the generated relative permeability data was not compared to the experimental one. Ramstad et al. (2012) simulated steady-state and unsteady-state experiments of two-phase flow using Lattice-Boltzmann on micro-CT images of Bentheimer and Berea samples. The results were in a good agreement with the reported experimental data, except non-wetting-phase relative permeability for drainage, which was calculated from production and pressure data; authors explained that with viscous instabilities (viscous fingering) which contradict Darcy's law assumptions for two-phase flow. Raeini et al. (2015) tried to study capillary trapping effect by solving full Navier-Stokes equations for two-phase flow on micro-CT images of Berea sandstone and LV60 sandpack, and compared the results with the experiment and quasi-static PNM simulation. One of the common problems encountered during Lattice-Boltzmann-based simulations of two-phase flow is wetting film thickness being smaller than voxel size, which can lead to erroneous results. (Raeini et al., 2015, Ahrenholz et al., 2008, Vogel et al., 2005)

The other disadvantage of Direct Simulation methods is much smaller scale of simulation compared to PNM, while PNM simulations can go up to close to core scale (Blunt et al., 2013).

In Pore-Network Models (PNM) — the second group of models — the pore space is characterized by a network of pores connected by throats with idealized and constant cross-sectional geometries. Researchers have used different cross-sectional shapes including circle, triangle, square, rectangle, star, and ellipse. Such simple geometries are particularly chosen to calculate the corresponding threshold capillary pressures of displacements using more computationally efficient analytical approaches. This is

because ‘threshold capillary pressures’ and ‘phase connectivities’ are primarily used to determine displacement sequences at pore levels. Most pore network models are developed under quasi-static conditions where capillary forces are solely responsible for fluid displacements at pore levels (Blunt et al. 2002, 2013; Piri and Blunt 2005a, Zolfaghari 2017a, 2017b). This assumption is reasonably valid when we determine the key forces controlling the physics of flow through porous media. At the pore scale level, due to very small fluid velocities, viscous forces become negligible compared to capillary forces (Satter and Iqbal 2015). Despite that fact, researchers have also been able to expand the capability of Pore-Network Models to incorporate viscous and gravitational forces (Joekar-Niasar et al. 2010, Sheng and Thompson 2013, Aghaei and Piri 2015). Although there is a still a lot of discussion around the experimental validation of the results obtained from PNM simulation (Oren 1997, Piri and Blunt 2005b, Piri and Karpyn 2007, Aghaei and Piri 2015, Zolfaghari and Piri 2016, Yang 2017), the latest model with the cooperative pore-body filling presented by Ruspini et al. 2017 showed the capability of the PNM to predict the experimental measurements. In addition, the research has been done by Miao et al. (2017) to create a pore network without pore shape simplifications. In that model single-phase hydraulic conductance of the actual pore element (without idealization of geometry) is predicted by the Neural Network based on three parameters describing a pore element: circularity, elongation and convexity. Using CFD, Navier-Stokes equation was solved and hydraulic conductance data was generated for 3292 pore elements and was used to train the Neural Network. 90% of hydraulic conductance predictions lied within an accuracy of ±20%. This might be the first step in creating a model which would combine both accuracy and efficiency at the same time.

Considering the advantages that PNMs can offer in comparison to direct methods, one can find them more suitable for the purpose of studying the electrical and transport properties of carbonates.

However, characterization of the carbonate rocks still remains challenging due to the existence of complex multiscale pore structures and their connectivity. This causes considerable heterogeneity at different scales presenting a tough challenge for engineers and geologists in determining the performance of the carbonate reservoirs. One of these challenges comes from the fact that most of the traditionally used models for studying transport and electrical properties are developed for siliciclastic rocks which may give erroneous results when being applied to carbonates (Talabani et al. 2000; Doveton 2001; Bauer et al. 2011; Prodanovic et al. 2014). Depositional history of carbonate rocks makes them completely different from siliciclastic rocks (Akbar et al. 2000; Ahr 2011). The latter ones are composed of pieces (usually, well-sorted) of the other rocks that were eroded by weathering processes, while most of the carbonates are made up from the fragments of calcareous organisms (Akbar et al. 2000). Therefore, one can expect more homogenous pore space in clastic rocks than in carbonates. Later diagenetic alterations drastically increase heterogeneity which is likely to occur in carbonates due to their brittle nature and vulnerability of their minerals to dissolution (Akbar et al. 2000; Bear et al. 2012). This causes the pore space in carbonates to undergo various morphological changes, ultimately, becoming very heterogeneous. Thus, carbonates contain not only interparticle but also intraparticle porosity. The latter is usually referred to as microporosity. The recent works have shown that microporosity can account for a very significant portion of the pore space in carbonates which emphasizes the importance of

its effect on the electrical and transport properties of these rocks (Norbisrath et al. 2015; Gundogar 2016).

Traditional techniques used in Digital Rock Physics also fail to provide an accurate pore space description for carbonates because of their extreme heterogeneity within a small volume. The challenge arises due to the selection of an appropriate scale that represents their wide pore size distributions. Regardless of the resolution, pore sizes in the microporosity zones are often below the resolution of the tool being used (Blunt et al. 2013; Bultreys et al. 2015). On one hand, a 3D image of porous media should cover a larger volume than its Representative Elementary Volume (REV). On the other hand, it should have high enough resolution to capture smaller pores. That causes the problem of scale where sub-resolution microporosity regions exist in pore-scale images regardless of the imaging technique being employed (e.g., micro-CT scanning). Since pore space topology cannot be captured in these unresolved regions, they are often ignored in the pore-scale models. Assuming microporous zone as a void space or as a nonporous solid will result in incorrect predictions of flow and electrical properties such as absolute and relative permeabilities, capillary pressure, and formation factor (Bultreys et al. 2015; Norbisrath et al. 2015; Soulaine et al. 2016). It should be noted that for monomineralic rocks, although individual micro-pores cannot be imaged, the regions with microporosity can be identified based on their gray level range on gray-scale images of the pore space (Bultreys et al. 2015).

Chapter 2. Literature Review

Over the last few years, there have been several attempts to develop modeling techniques for studying microporosity and its impact on the flow and electrical properties. Particularly, some researchers have tried to incorporate microporosity into the PNMs (Prodanovic et al. 2014, Bultreys et al. 2015). To incorporate microporosity regions, one should obtain a 3D image of an REV (or a larger volume) that has high enough resolution to capture micro pores. This would generate a huge amount of voxels which is beyond the processing capabilities of the modern computers (Jiang et al. 2013). Several authors have tried to circumvent capturing the actual pore space of microporosity by modifying PNMs to accommodate different scales. Table 2.1 provides a brief overview of the approaches that have been used to model microporosity.

Bekri et al. (2005) introduced one of the first dual PNMs with a lattice network of macro pores and parallel microporous matrixes. To model the flow, upscaled known properties were assigned to the matrix including porosity, permeability, capillary pressure, and relative permeability curves. Bauer et al. (2011, 2012) followed the same approach by modeling microporous zones as the blocks of continuous porous media. In their work, each block connects two macro pores parallel to the linking macro-throat. Jiang et al. (2013) built multi-scale pore networks with individual pores for microporosity zones. In their model, representative networks were first generated from images at distinct length scales. A stochastic method was then used to generate a larger network based on the statistical information gathered from networks of different scales.

Work	Overview	Disadvantages	Advantages (over predecessor)	Electrical properties
Bekri et al. 2005	Vugs/fractures are modelled as a lattice network of macro pores with the microporous matrix, the microporous zone is treated as continuous porous media	• Microporosity acts only in parallel • Only drainage was modeled • Does not contain pore networks for microporous zones	As all PNMs, has less computational time in comparison with direct models / Less complex	Modeled
Bauer et al. 2011, 2012	Microporous zones are represented as blocks of continuous porous media connecting 2 macro pores that are already connected through a macro throat	• Microporous zones are connected to macro pores only in parallel • Does not contain pore networks for microporous zones, microporosity is modeled as continuous porous media	Crevice flow was modeled	Modeled
Jiang et al. 2013	Actual pore network for a random microporosity zone is generated and used to generate a larger pore network that would fit the macro network domain	Impractical computational cost and time	• Better representation of microporosity/ individual micro pores • Better representation of cross-scale connectivity	Not Modeled
Prodanovic et al. 2014, Mehmani and Prodanovic 2014	A copy of macro network reduced in size and mapped on microporous zones	Crevice flow of the wetting phase not modeled	A model with individual micro pores, without upscaling	Not Modeled

Table 2.1. Overview of the approaches used to model microporosity.

Work	Overview	Disadvantages	Advantages (over predecessor)	Electrical properties
Bultreys et al. 2015	Extension of the previous approaches with upscaled microporosity, parallel connection added	• Only drainage was modeled • Assumption: any number of pores touching the same microporous zone are connected, i.e. microporous zone can percolate in any direction	Microporosity zones are connected to macroporosity both parallel and in series	Modeled
Soulaine et al. 2016	Direct modeling; flow was modeled using Darcy law for the microporous zone, Stokes–for macro pores	• Computationally costly • No multiphase flow	Better preservation of the actual locations of microporosity	Not modeled

Table 2.1. (continued). Overview of the approaches used to model microporosity.

Prodanovic et al. (2014) tried to replace microporous zones with a downsized copy of a macro network generated from the resolvable pore space. They systematically investigated the effects of microporosity on transport properties. But their model did not include crevice flow of the wetting phase. That means that the non-wetting phase would completely displace the wetting phase during drainage without leaving any wetting layers in the crevices. This overestimates electrical resistances at low water saturations since piston-like displacements during drainage would disrupt continuity of the conductive aqueous phase. The absence of the wetting phase in corners also eliminates snap-off displacements which reduce trapped oil saturation and electrical resistances during the course of an imbibition process. In this work, we use the pore-scale network model presented by Zolfaghari and Piri (2014, 2017a) that does allow wetting phase to reside in the crevices of angular pores and is capable of simulating the associated displacements

such as snap-off. Bauer et al. (2011) pointed out the importance of wetting layers for accurate modeling of electrical properties. They showed that resistivity index is hugely overestimated for Fontainebleau sandstone when the wetting film is not modeled. Besides sandstone, they investigated the electrical properties of carbonates with a major limitation in their model: microporous zones were only connected in parallel to the macro pore networks. Bultreys et al. (2015) have also used a similar approach of treating microporosity as a continuous porous media and assigning upscaled properties. However, they allowed both parallel and in-series connections for the linking of microporosity zones to macro pore networks. In these works, the upscaled properties are usually estimated based on the gray level of microporous zones, which is valid only for monomineralic rocks (Bultreys et al. 2015).

Besides PNMs, direct modeling techniques have been also used for fluid flow modeling in the pore space of various rock samples (Blunt et al. 2013; Bultreys et al. 2016). As was mentioned, these techniques use an actual geometry of the pore space (i.e., without simplifications of the pore networks) to solve governing equations of flow. Microporosity still remains a challenge due to being unresolved. Recently, Soulaine et al. (2016) used a direct model consisting of Stokes equation for macro pores and Darcy equation for microporosity regions. Authors successfully calculated absolute permeability of Berea sandstone from images with 2% subresolution porosity. They reported 60% overestimations of the permeability for the cases where microporous zones are mistakenly replaced with the void space. As mentioned, microporosity greatly impacts transport and electrical properties of samples with wide pore size distributions (Bekri et al. 2005; Bauer et al. 2011, 2012). The specific problem associated with the electrical

properties has been also referred to “Low Resistivity Pay” (LRP) phenomenon in the oil and gas industry (Boyd et al. 1995, Coates et al. 1999). Formation resistivity is often measured during well logging operations which is then correlated to the water saturation. This water could be however mobile, partially mobile, or immobile. In LRP zones, the assumption of high mobile water saturation leads to underestimation of hydrocarbon resources (Coates et al. 1999). This could be caused by the existence of microporosity or conductive minerals (Boyd et al. 1995). Differentiation of bound water from mobile water in carbonates is another research topic by itself. The primary focus of this work is however to investigate the effect of microporosity on electrical properties.

It is worth mentioning that microporosity does not have universal quantitative or qualitative definition. Various authors characterized it differently (Rahman et al. 2011). Choquette and Pray (1970) defined micropores as pores smaller than 1/16 mm (≈62 μm) in diameters. Swanson (1985) described micropores as pores which do not contribute to rock’s permeability due to their significantly smaller sizes. Cantrell and Hagerty (1999) set the upper limit of 10 microns, identifying microporosity as the difference between total measured porosity and visible porosity from thin section analyses. Similarly, Ehrenberg et al. (2015) defined micropores as pores not visible in their petrographic analysis (< 30 μm). As mentioned, in Digital Rock Physics, microporosity is usually defined as any pores below the resolution of the imaging tool being used (Blunt et al. 2013, Bultreys at al. 2015). In this work, we consider and refer to any pores below the resolution of the imaging tool as “micropores”. The goal of this paper is to systematically investigate the effect of microporosity and its uncertain properties on electrical and flow properties of porous media using PNMs. To incorporate microporosity into our networks, we generate two

types of pore networks, i.e., macro- and micro-pore networks. These two types of networks are later being linked by a special random cross-scale connection algorithm. We assume networks are strongly water-wet and originally fully saturated with water. Oil is then injected during primary drainage by calculating threshold capillary pressures of all available oil-to-water displacements. Primary drainage mimics migration of the oil into reservoir during which oil/water capillary pressure increases. Specifically, we extend the capability of the model developed by Zolfaghari and Piri (2017a, b) to take into account microporosity and calculate electrical properties of a rock sample. The model simulates crevice flow using two main displacement mechanisms at pore levels, i.e., piston-like and snap-off displacements. The detail of these displacements is described elsewhere (Piri 2003, Piri and Blunt 2005, Zolfaghari 2014).

Chapter 3. Methods

3.1. Quasi-static Pore-Network Modelling Simulations of Primary Drainage and Imbibition

Pore Network Modelling is one of the most popular and practical methods for the simulation of multiphase flow at the pore scale due to its computational efficiency and incorporated level of physics such as layer and crevice flows. In these models, pore space is represented by a simplified network of pores and throats with a constant cross-sectional shape for each element. Each element is assigned a different shape, inscribed radius, length, and spatial coordinate. These models are originally developed for the capillary-dominated flow regimes, where pore-level fluid/fluid displacements are determined based on capillary forces (Blunt et al. 2002, 2013; Piri and Blunt 2005a, Zolfaghari 2017a,

2017b). Although these models use idealized networks to represent the actual pore space, many studies have shown their capabilities for predicting experimental measurements (Oren 1998, Piri and Blunt 2005b, Piri and Karpyn 2007, Aghaei and Piri 2015, Zolfaghari and Piri 2016, Yang 2017, Ruspini et al. 2017). PNM techniques have also been used to investigate biomass growth, dissolution/precipitation and adsorption processes (see Xiong 2016 for more references). Here in this work, we assume capillary-dominated flow regime in all of our generated networks. Pores and throats in our 2D networks have regular triangular cross sections while those in our 3D networks have a wide range of shapes (i.e., circle, irregular triangle, and square). All the pore-networks used in this work are assumed to be strongly water-wet with the receding and advancing oil-water contact angles of 0 and 10°, respectively.

In two-phase system consisting of oil and water phases, pressure difference across oil and water interface can be calculated using Young-Laplace equation:

$$P_o - P_w = \sigma_{ow}\left(\frac{1}{r_1} + \frac{1}{r_2}\right) \tag{1}$$

Where P_o and P_w are the pressures of oil and water phases respectively, r_1 and r_2 are principal radii of curvature of the oil-water interface.

The threshold capillary pressures are calculated based on MS-P theory (introduced by Mayer and Stowe and developed further by Princen). For a closed thermodynamic system with *m* phases which are in thermodynamic equilibrium and are completely immiscible, Helmholtz free energy (*dF*) can be defined as

$$dF = -\sum_{i=1}^{m} P_i dV_i + \sum_{ij=12,13,\ldots 23,24,\ldots}^{\frac{m!}{2(m-2)!}} \sigma_{ij} dA_{ij} \qquad (2)$$

where P_i is the pressure and dV_i is the change in the volume of *i*-th phase, σ_{ij} is the interfacial tension and A_{ij} is the surface area of the contact between phases *i* and *j*.

For two-phase system consisting of oil and water this equation can be written in the following way:

$$\mathrm{dF} = -\mathrm{PdV_o} - \mathrm{P_w dV_w} + \sigma_{os}\mathrm{dA_{os}} + \sigma_{ws}\mathrm{dA_{ws}} + \sigma_{ow}\mathrm{dA_{ow}} = 0 \qquad (3)$$

Since the system is closed, the change in water-solid contact area equal to the change in oil-solid contact area and change in water volume equals the change in oil volume, therefore, those parameters can be factored out:

$$\mathrm{dA_{ws}} = -\mathrm{dA_{os}}$$

$$\mathrm{dF} = -\mathrm{P_o dV_o} - \mathrm{P_w dV_w} + \mathrm{dA_{os}}(\sigma_{os} - \sigma_{ws}) + \sigma_{ow}\mathrm{dA_{ow}} = 0$$

$$-\mathrm{dV_w} = \mathrm{dV_o}$$

$$\mathrm{dF} = \mathrm{dV_o}(-\mathrm{P_o} + \mathrm{P_w}) + \mathrm{dA_{os}}(\sigma_{\mathrm{os}} - \sigma_{\mathrm{ws}}) + \sigma_{\mathrm{ow}}\mathrm{dA_{ow}} = 0$$

And since $\mathrm{P_{cow}} = \mathrm{P_o} - \mathrm{P_w}$:

$$\mathrm{dF} = -\mathrm{P_{cow}}\,\mathrm{dV_o} + \mathrm{dA_{os}}(\sigma_{os} - \sigma_{ws}) + \sigma_{ow}\mathrm{dA_{ow}} = 0$$

According to Young's equation $\sigma_{os} - \sigma_{ws} = \sigma_{ow}\cos\left(\theta_{ow}^{receding}\right)$, therefore:

$$\mathrm{dF} = -\mathrm{P}_{cow}\,\mathrm{dV}_o + \sigma_{ow}\cos\left(\theta_{ow}^{\mathrm{receding}}\right)\mathrm{dA}_{os} + \sigma_{ow}\mathrm{dA}_{ow} = 0$$

$$\mathrm{dF} = -\mathrm{P_{cow}}\,\mathrm{dV_o} + \sigma_{ow}\left[\cos\left(\theta_{ow}^{\mathrm{receding}}\right)\mathrm{dA_{os}} + \mathrm{dA_{ow}}\right] = 0$$

Since $\mathrm{P_{cow}} = \sigma_{ow} \times \frac{1}{r_{ow}}$:

$$\frac{-dA_o}{r_{ow}} + dL_{ow} + \cos(\theta_{ow})dL_{os} = 0 \quad (4)$$

The developed model in this work can be divided into two main parts: a pore network generator and a flow simulator. This is to investigate microporosity's impact on flow and electrical properties using both 2- and 3-D pore networks. The 2D pore networks are generated to interpret the results on simpler networks. We then compare our results of 3D pore networks extracted for Berea sandstone and Estaillades limestone samples. Here, we go over our pore network modeling and generation techniques.

3.2. 2D pore networks generation

Being able to generate a random Pore-Network model allows to have control on several geological or geometrical properties such as porosity, pore coordination number and pore size range.

One of the main challenges in generation of random pore-network model is making it geometrically and geologically realistic, so that lengths and radii are within pre-given ranges and within geometrical limitations. Therefore, we generate a random pore-network on lattice principle. All pores are located in the nodes of lattice and all throats are located on the sides of a grid cell, thus, the network has vertical and horizontal throats.

Here, we refer to pores and throats altogether as 'elements'. In the context of Python code, all elements are instances of the same class named 'Triangle'. Triangle class takes two input parameters: inscribed radius and length. All other parameters such as threshold

capillary pressure and water saturation at some given capillary pressure are automatically calculated and stored as attributes of a triangular element. Each element has inscribed radius and length assigned to it.

All the throats are numbered by even numbers starting from 2, all the pores are numbered by odd numbers starting from 1. The whole lattice pore-network is generated in the form of matrix. This makes it easy to identify which element(s) each element is connected to. Below you see example matrix (Fig. 3.1) generated for a lattice pore-network of the size 5-by-4, which means it has 5 pores in every column and 4 pores in every row. ‘nan’ stands for ‘not a number’ and does not contain pore or throat.

2	1	20	11	38	21	56	31	74
nan	12	nan	30	nan	48	nan	66	nan
4	3	22	13	40	23	58	33	76
nan	14	nan	32	nan	50	nan	68	nan
6	5	24	15	42	25	60	35	78
nan	16	nan	34	nan	52	nan	70	nan
8	7	26	17	44	27	62	37	80
nan	18	nan	36	nan	54	nan	72	nan
10	9	28	19	46	29	64	39	82

Figure 3.1. Example matrix generated for a 2D pore-network numbering.

All elements have a shape of equilateral triangle (Fig. 3.2). Pore network generator creates 2D pore networks readable for the flow simulator module. Flow simulator can read any 2- or 3-D network and simulate fluid-fluid displacements during two- and three-phase flow conditions. To illustrate the impact of microporosity, less complex topologies are considered by creating pore networks on regular rectangular 2D lattices where all pore centers lie in the same plane.

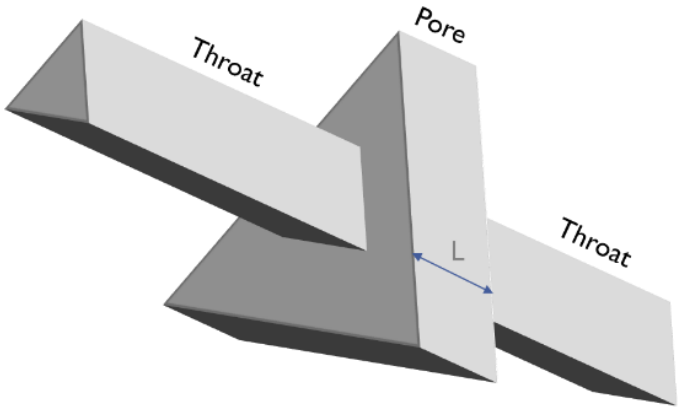

Figure 3.2. Illustration of the equilateral triangular pore and two throats with the same cross-sectional shape connected to it. L is used to denote the length of the pore.

To generate these 2D lattice networks, we assign the same distances between pore centers both horizontally and vertically. We then randomly distribute variable pore sizes throughout the network ensuring that pores can geometrically fit on the lattice (Fig. 3.3).

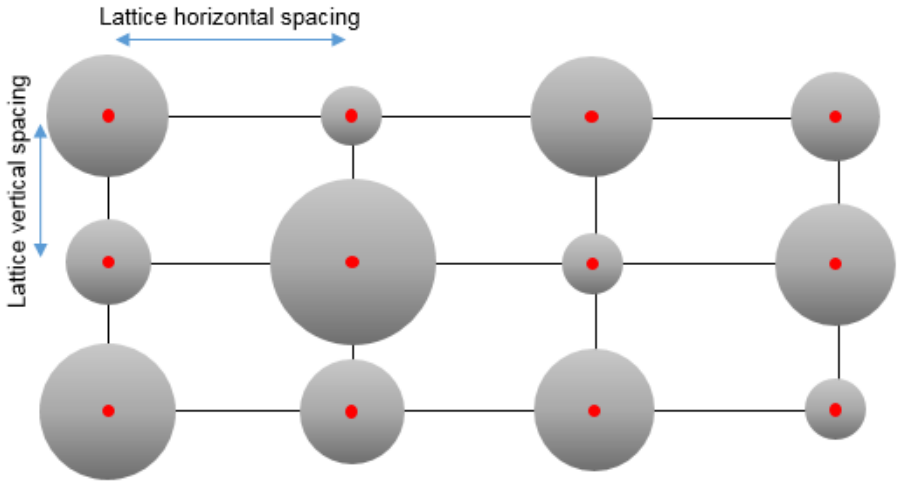

Figure 3.3. Illustration of a 2D lattice pore network where red dots represent pore centers (Hakimov et al. 2018). Reprinted by permission of Copyright SPE.

Lattice horizontal spacing (*LaHS*) is defined as the horizontal distance between centers of two neighboring pores which is equal to the sum of half-lengths of two connected pores and their connecting throat's length. The vertical distance between centers of two neighboring pores, however, is referred to as lattice vertical spacing (*LaVS*). It consists of inscribed radii of two connected pores and their connecting throat's length. The corresponding equations for *LaHS* and *LaVS* are:

$$LaHS = \frac{L_{pore\ i}}{2} + L_{connecting\ horizontal\ throat} + \frac{L_{pore\ j}}{2} \qquad (5)$$

$$LaVS = IR_{pore\ i} + L_{connecting\ vertical\ throat} + IR_{pore\ j} \qquad (6)$$

LaHS and *LaVS* may not necessarily be equal. They are randomly chosen from the ranges calculated based on the given pore/throat size distributions. Assuming minimum and maximum values for each parameter in the above equations, the following inequalities can be obtained:

$$(L_{throat})_{min} + (L_{pore})_{min} < LaHS < (L_{throat})_{max} + (L_{pore})_{max} \qquad (7)$$

$$(L_{throat})_{min} + 2 \times (IR_{pore})_{min} < LaVS < (L_{throat})_{max} + 2 \times (IR_{pore})_{max} \qquad (8)$$

Once lattice spacing is fixed, pores and throats are populated based on the given pore/throat size distributions. In all generated 2D networks, each pore or throat is a triangular prism with the cross-sectional shape of an equilateral triangle. The volume of each prism is then calculated for every pore and throat.

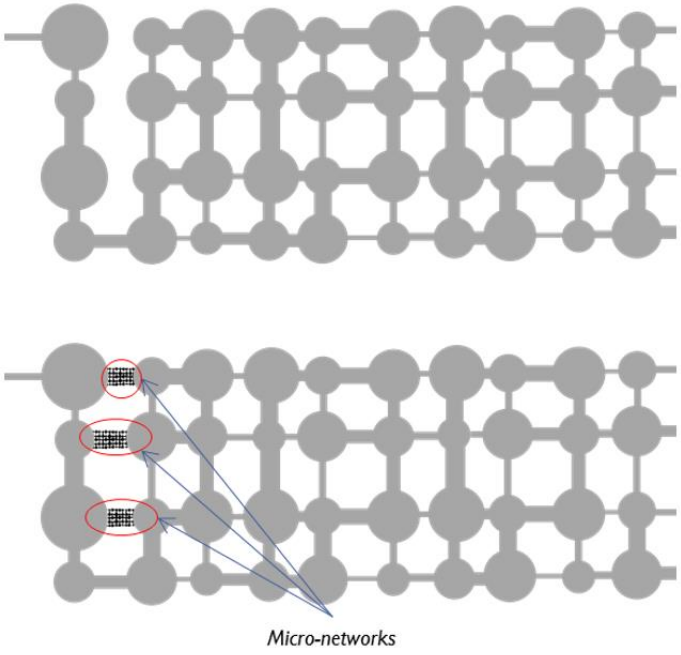

Figure 3.4. Two identical macro-pore networks: a small example of base pore network (top) and a modified pore network with microporosity (bottom) (Hakimov et al. 2018). Reprinted by permission of Copyright SPE.

To systematically investigate microporosity's impact on transport and electrical properties, we create two identical macro-pore networks. One of the networks is then further modified to include microporosity by adding micro networks with smaller pore sizes (Fig. 3.4). Once again, all geometrical constraints are considered for the generation of these lattice micro networks. Specifically, we ensure that the inserted micro networks would fit between the two neighboring macro-pores. This allows us to generate geometrically realistic pore networks.

3.3. 3D pore-networks generation

3.3.1. Samples used in this work

The samples used in this work include one sandstone (Berea) and two carbonates — one outcrop (Estaillades limestone) and one reservoir carbonate. The latter one was obtained from the oil-producing carbonate formation of Osagean age of Mississippian period in STACK play in Oklahoma. Conventional techniques used for water saturation calculation yielded a high value for the considered interval. However, the Special Core Analysis (SCAL) indicated the opposite (lower water saturation). Therefore, salinity was assumed to be very high to increase electrical conductivity used in empirical equations which would yield lower estimated value for water saturation. However, formation water analysis indicated invalidity of this assumption. Thus, the company operating the field has concluded from the well log interpretation and production tests the possibility of the presence of the Low Resistivity Pay zone in the formation.

3.3.2. 3D Image acquisition and segmentation

Micro-CT scanner with the imaging resolution of 3.1 μm was used to obtain 3D image of the interior of the rock sample (Fig. 3.5). X-rays pass freely through the pore space but are absorbed or scattered by the solid (matrix). The denser the solid, the more X-rays are attenuated. Microporous zones have smaller effective density than the regular imporous solid parts of the sample and, therefore, are supposed to cause less attenuation of the X-rays and appear less bright on CT-scan images. This assumption is reasonably valid for carbonates since they are mono-mineralic rocks. The mineralogy analysis of the reservoir carbonate sample has shown that calcite comprises approximately 97% of the sample.

The picture below shows unsegmented, unfiltered original 3D image of the Osage carbonate sample (Fig. 3.5. (A)). Black voxels represent resolvable pore space (hereinafter, referred to as “macroporosity”), while dark grey ones correspond to microporous zones, and contain pore space and solid phase at the same time. After obtaining the 3D image of the sample, the image was filtered and segmented based on grey level (Fig. 3.5. (B)).

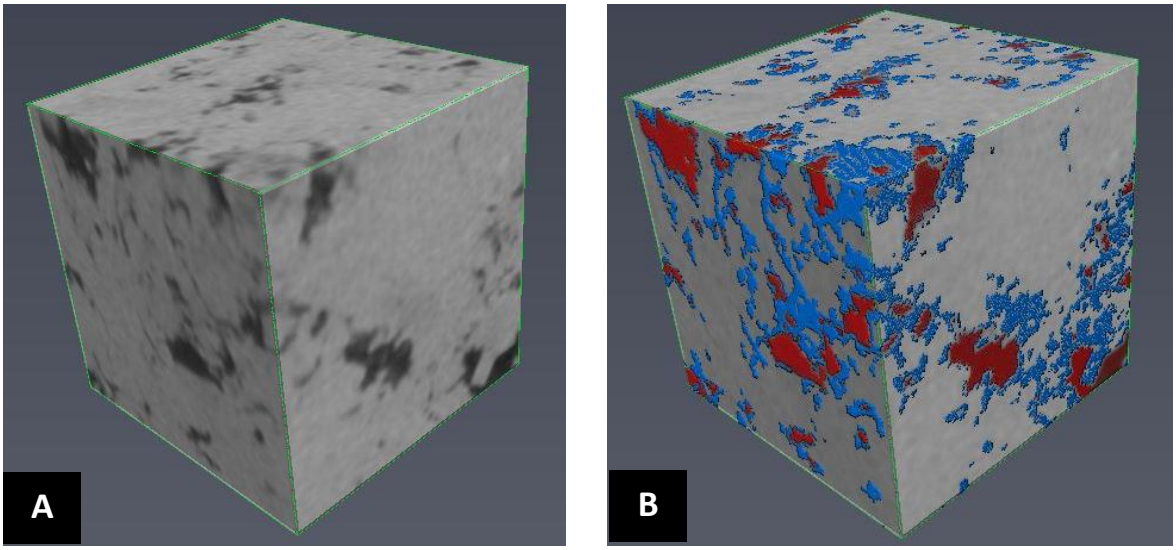

Figure 3.5. The raw 3D micro-CT scan image of the sample with the resolution of 3.1 μm (A), phases extracted the image segmentation overlaid on the original micro-CT scan image after (B): blue color represents microporosity, red — macro pore space.

Image segmentation is a process when voxels of the image are extracted based on the given grey level range. For this specific case, the 3D image was segmented into three “phases”: microporosity, macro pore space and solid phase. Microporosity is assumed to have intermediate grey level, since pore space(void) is represented by the minimum value and the solid phase — by the maximum value of the obtained data. The Figure 1B shows

the extracted macro pore space and microporous zones overlaid onto the original micro-CT scan image.

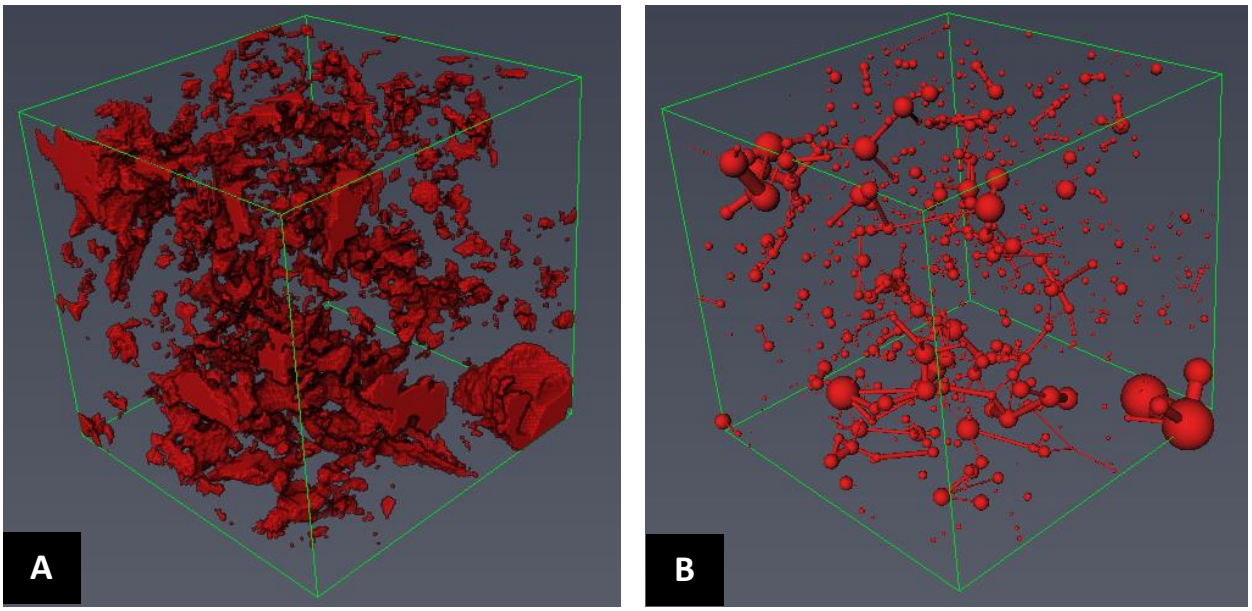

Figure 3.6. Resolved (macro) pore space (A) and its corresponding pore network where pore and throat radii demonstrate largest inscribed radii (B).

The extracted macro space is then used to generate a macro Pore Network Model. As can be seen from the Fig. 3.6., the significant portion of the macro pore space is unconnected and therefore, the pore-network generation algorithm yields a large number of isolated pores or clusters of pores. This again emphasizes the importance of inclusion of the micro pore-networks into the model, since the individual isolated macro pores might be connected through micro pore-network. Connection between macro and micro pores will be referred to as ‘cross-scale’ connection and is discussed in the following subsection.

3.3.3. Stochastic pore-network generation

After the macro pore-network has been generated, the next step is to identify spatial location and geometrical dimensions of the microporous zones. As was already

mentioned, microporous zones are treated as a separate phase and have a separate range of grey level which must be more than maximum grey level value of void phase (pore space) and less than minimum one of the solid phase. Extracting the voxels in that range, a *pseudo pore space* is obtained. After having the microporous media (pseudo pore space) extracted, in an analogical way to pore-network model generation, microporous media is converted into a network of idealized geometrical figures that would reasonably capture the same volume and dimensions of microporous clusters, and be located in the same geometrical domains. This network will be referred to as 'a pseudo-network'. Having the information on the physical dimensions, volume and location of the elements of the pseudo-network, a special code has been developed that would stochastically generate micro pore-network within the geometrical space occupied by the pseudo-network (Fig. 3.7).

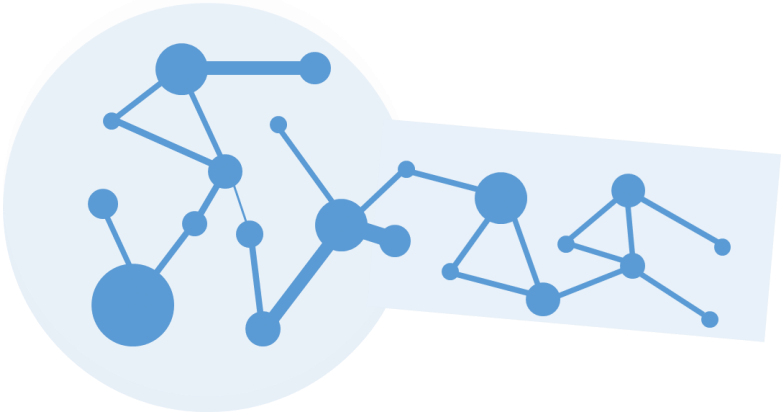

Figure 3.7. Illustration of a micro pore network generated within the pseudo pore space (network).

As can be seen from the Fig. 3.8 microporous zones cover almost the whole domain of the rock sample which indicates the high chance of them being in contact with macro pores.

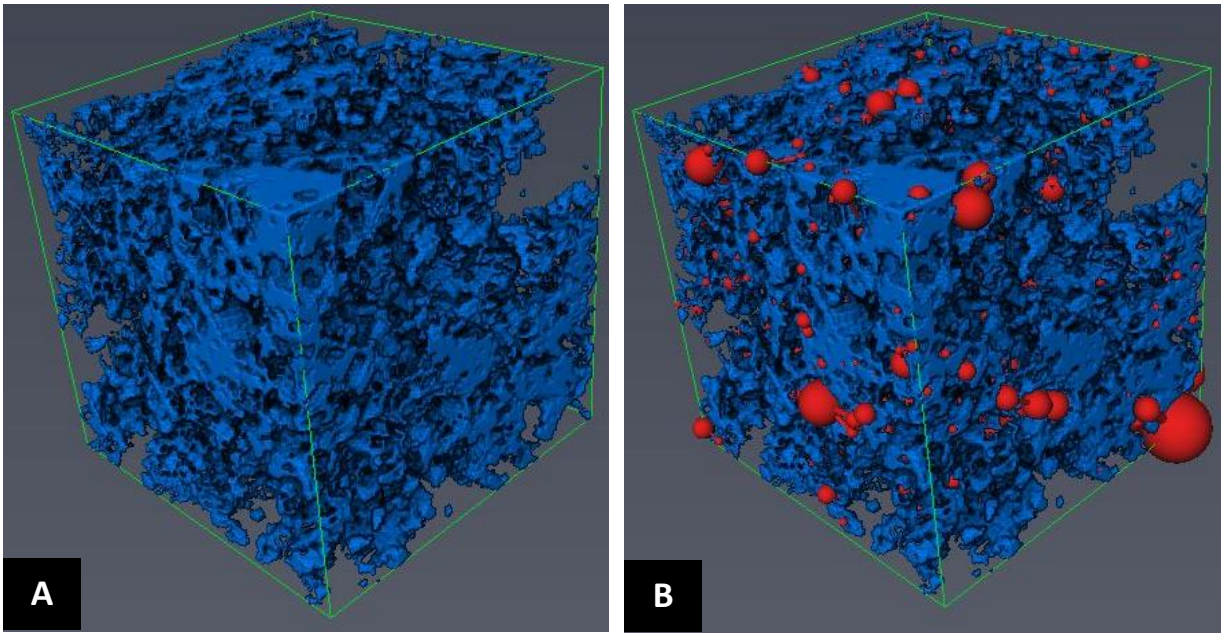

Figure 3.8. The segmented microporosity zone (A) and its overlay with the extracted pore network of the resolved pore space (B).

There are many unknowns associated with microporous zones, such as porosity and pore size distribution. Therefore, there are numerous possible networks than can be generated within the geometrical space occupied by microporous zones.

The algorithm used in this model provides more flexibility and allows to vary various input parameters such as pore size distribution, local porosity in microporosity zone, pore coordination number distribution and max throat length.

In order to study the sensitivity of the results to various parameters, various micro pore-networks have been generated with different porosities, pore size and pore coordination number distributions. In this paper, we present the results for 15 cases with different micro pore-networks. All these cases can be grouped based on the pore size distribution used for microporosity zones. A group of networks with the small-sized micro pores will be

referred to as ‘S-networks’, with the medium-sized pores — as ‘M-networks’ and so on (Table 3.1).

	Small PSD	Medium PSD	Large PSD
Target porosity in microporous zones:	Distribution type: normal Mean pore size=2.5 µm Standard Deviation=0.5 µm	Distribution type: normal Mean pore size=4.5 µm Standard Deviation=0.5 µm	Distribution type: normal Mean pore size=6.5 µm Standard Deviation=0.5 µm
10%	S-10	M-10	L-10
20%	S-20	M-20	L-20
30%	S-30	M-30	L-30
40%	S-40	M-40	L-40
50%	S-50	M-50	L-50

Table 3.1. All the generated pore-networks named based on the pore size and porosity.

Before we proceed with the explanation of pore-network generation algorithm some terms should be made clear in order to avoid confusion. First of all, target porosity is the desired local porosity within microporous zones that the model is trying to achieve by the end of the stochastic pore-network generation. This porosity should not be confused with incremental microporosity or total porosity. In order to avoid any confusion, the difference between terms is illustrated in the example further below (Fig. 3.9). If, for example, the pore space occupies 50% of the bulk volume (i.e. macroporosity=50%) and microporous zone – 25%, then incremental microporosity will be equal to a product of the local porosity and the fraction of the bulk volume that microporous zone accounts for — 0.25 (25%).

Generation of a micro-network matching specific properties within specific limited geometrical space is not a trivial task, i.e. not for any given constraints a micro-network with the desired properties can be generated. Different cases with different pre-set input parameters for a micro-network would involve a different set of challenges. Therefore, a lot of these challenges are addressed in stochastic micro-network generation through trial-and-error.

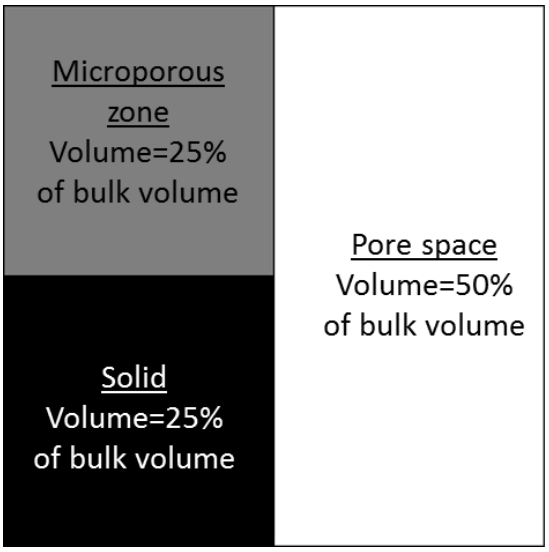

$$Incremental\ microporosity =$$

$$= \frac{Micro\ pore\ volume}{Bulk\ volume} =$$

$$= \frac{Local\ Porosity \times 0.25 \times Bulk\ Volume}{Bulk\ Volume} =$$

$$= Local\ Porosity \times 0.25$$

Figure 3.9. Explanation of the difference between terms 'local porosity' and 'microporosity'.

The whole general workflow can be briefly described by the following steps:

1) Construction of a macro pore-network based on the pore space resolvable on 3D image of the rock sample (Fig. 3.10(A)).
2) Extraction of the geometrical space occupied by microporosity in a form of a network.

3) Generation of the micro pores within the pseudo network based on the given target local porosity and PSD (micro throats volumes will be considered to be negligible and not used to match the local porosity).
4) Creating links (micro-throats) between micro-pores based on the pre-set target pore coordination number distribution and maximum throat length. It should be noted that before connection, a special algorithm ensures that 2 micro pores are located in the same microporosity cluster.
5) Cross-scale connection algorithm: the code randomly generates throats between macro pores and micro pores. However, each time, a throat connecting macro and micro pore is being generated only in the case when the following 2 criteria are met:
    a. The micro-pore is located within microporosity cluster that is “touching” the macro pore.
    b. Adding the connection between the given micro and macro pores would not exceed the assigned (target) coordination number for the given micro pore (the absolute tolerance is pre-set).
    c. The resulting throat length would not exceed the maximum allowed throat length (defined as an input parameter) for micro-to-macro connection (the relative tolerance is pre-set).
6) Continuous cluster construction algorithm checks for connectivity and identifies isolated cluster of networks (or pores) and establishes links between the closest 2 pores of different clusters. In order to reduce computation time, a maximum length is pre-defined for the throat connecting 2 isolated clusters.

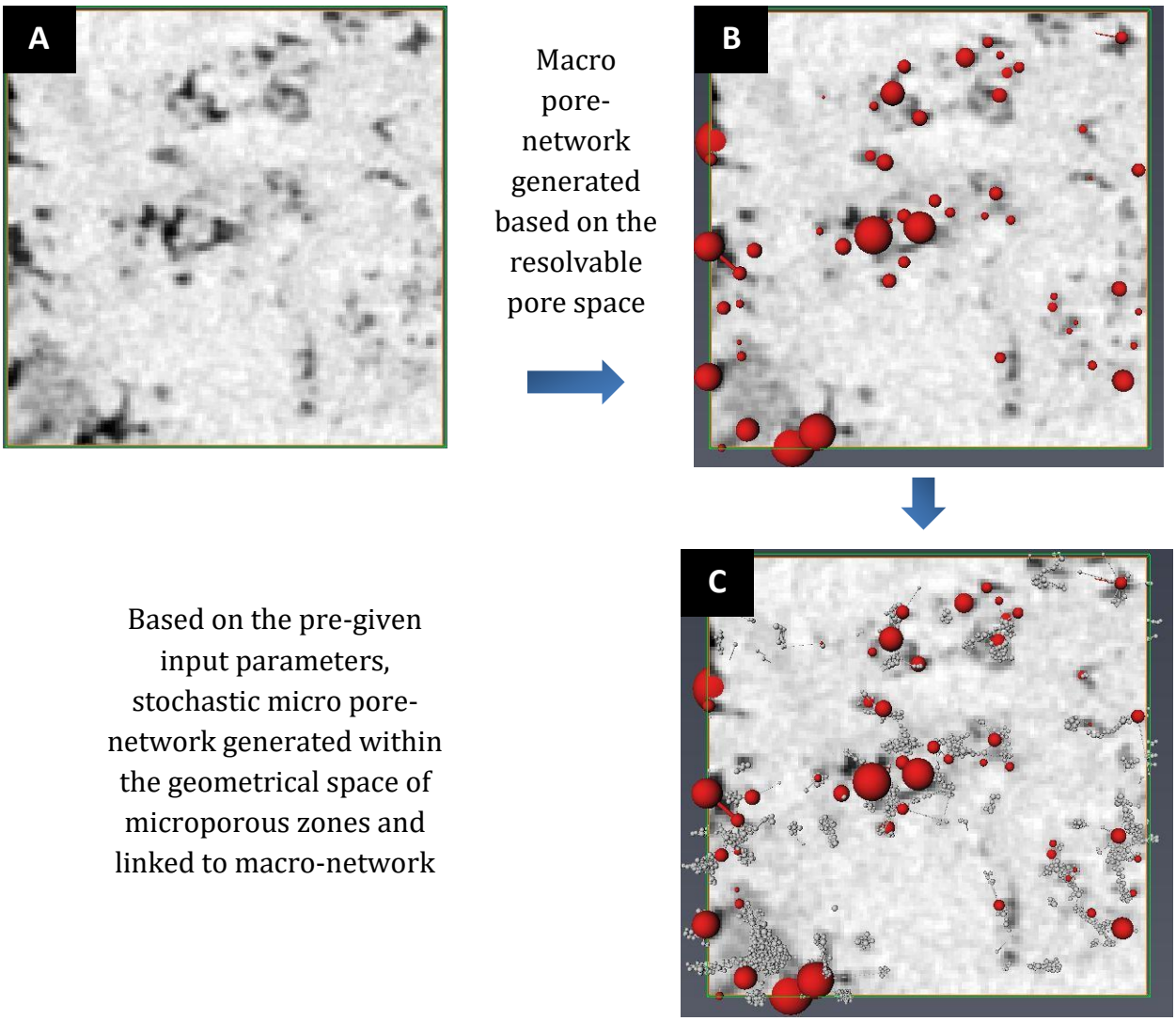

Figure 3.10. Illustration of the generated macro and micro networks and their locations in regard to the original 2D micro-CT scan image. First, an XZ-slice of the raw 3D micro-CT scan image is shown (A), then macro pores (red) are overlaid on top of the same slice (B). The last picture (C) shows the final network consisting of macro pores (red spheres) and stochastically generated micro pores (grey spheres).

After all these steps, the network construction is completed, and the final information is recorded and saved into pore-network files.

3.4. Calculation of electrical properties

As mentioned, we simulate multi-phase flow under capillary-dominated flow regime. This means that all fluid-fluid displacements are triggered by the change of capillary pressure between displacing and displaced phases during drainage and imbibition processes. The model calculates threshold capillary pressures of all potential displacements at each saturation. They are then compared against the overall capillary pressure of the network to determine occurring displacements. At each capillary pressure, after all the available displacements are done, a quasi-steady-state condition is reached. At this condition, all relevant transport and petrophysical properties such as water saturation, relative permeabilities, electrical resistance or resistivity, and resistivity index are calculated.

For a detailed description of the Pore Network Models and their constituent theories, the reader should see Piri and Blunt 2005a, Karpyn and Piri 2007, Blunt 2017, Zolfaghari and Piri 2017a. Here in this work, we specifically improve the model of Zolfaghari and Piri (2017a, 2017b) to estimate electrical properties in dual-porosity rock samples.

At each quasi-steady-state condition, electrical properties can be calculated in the similar way to transport properties (Bekri et al. 2005). Each of the transport properties has an analogical electrical parameter listed in Table 2. The analogical parameter to the hydraulic conductance is electrical conductance which is expressed as

$$g_e = \sigma_w \frac{A_w}{L} \qquad (9)$$

where A_w and L are water cross-sectional area and length of pore/throat, respectively. σ_w denotes electrical conductivity of brine and is assumed to be 54.645 S/m (Fleury 2004).

Transport property	Electrical property
Hydraulic conductance, g_h	Electrical conductance, g_e
Pressure, *P*	Electric potential, *U*
Flow rate, *Q*	Electric current, *I*
Absolute permeability, *k*	Formation Factor, *FF*
Relative permeability to water, $\boldsymbol{k_{rw}}$	Resistivity Index, *IR*

Table 3.2. The analogy between transport and electrical properties (Hakimov et al. 2018). Reprinted by permission of Copyright SPE.

Analogical equations for the electric (*I*) and hydraulic (*Q*) fluxes between 2 neighboring pores (*i* and *j*) are written as:

$$Q_{ij} = (g_{ij})_h \times \left(P_i - P_j\right) \quad \leftrightarrow \quad I_{ij} = (g_{ij})_e \times \left(U_i - U_j\right) \qquad (10)$$

Similar to the flow rate for permeability calculation (see, for instance, Piri and Blunt 2005), the summation of the inflow and outflow of the electric fluxes is zero in each pore (Fig. 3.11). This is consistent with Kirchhoff's current law under steady-state conditions. Substituting electric currents with $(g_{ij})_e \times (U_i - U_j)$ in the flux equation of each connected pore would yield *N* linear equations with *N* unknowns where *N* is the number of connected pores in the network. Thus, a matrix of electrical conductances is built to solve for the unknown parameters, i.e., electrical potentials of the connected pores. This covers all electron pathways throughout the pore network. Having electrical potentials, we calculate total electrical current going through the network at 100% water saturation.

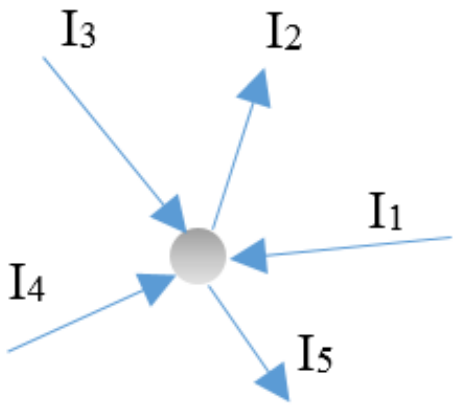

$$I_1 + I_2 + I_3 + I_4 + I_5 = 0$$

Figure 3.11. Kirchhoff's current law under a steady-state condition for a pore with the coordination number of 5 (Hakimov et al. 2018). Reprinted by permission of Copyright SPE.

This is used to find electrical conductivity of the whole network fully saturated with water using Eq. 11:

$$\sigma_{network\ @\ Sw=100\%} = \frac{I_{total\ @\ Sw=100\%} \times L_{network}}{A \times \Delta U} \qquad (11)$$

Formation Factor can then be determined as the ratio of electrical conductivity of brine to the electrical conductivity of the network:

$$FF = \frac{\sigma_{brine}}{\sigma_{network\ @\ Sw=100\%}} \qquad (12)$$

Electrical Resistivity Index (IR) is the ratio of the network's electrical conductivity at S_w=100% to the electrical conductivity at a given saturation. This can be further simplified to the ratio of total currents:

$$IR = \frac{\sigma_{network\ @\ Sw=100\%}}{\sigma_{at\ given\ Sw}}$$

$$= \frac{I_{total\ @\ Sw=100\%} \times L_{network}}{A \times \Delta U} \times \frac{A \times \Delta U}{I_{total\ at\ given\ Sw} \times L_{network}} =$$

$$= \frac{I_{total\ @\ Sw=100\%}}{I_{total\ at\ given\ Sw}} \qquad (13)$$

As mentioned, we generate networks of the same lengths and cross-sectional areas to investigate the impact of microporosity. Having networks with the same spatial dimensions, it is sufficient to compare only electrical conductances (g_e) or resistances (*R*) rather than conductivities (*σ*) or resistivities (*ρ*). The corresponding equations are presented below to further illustrate such reasoning:

$$\sigma_{network} = \frac{I_{total}}{\Delta U} \times \frac{L_{network}}{A} \qquad (g_e)_{network} = \frac{I_{total}}{\Delta U} \qquad (14)$$

$$\rho_{network} = \frac{\Delta U}{I_{total}} \times \frac{A}{L_{network}} \qquad R_{network} = \frac{\Delta U}{I_{total}} \qquad (15)$$

3.5. Tortuosity calculations

Generally, there are several types of tortuosity. All types, except geometrical, are related to some hydraulic, electrical or diffusive property. Geometrical tortuosity is independent of any transport process happening in the porous media and is solely a function of the pore structure. It is determined as the ratio of the shortest pathway length within the pore space between 2 points to the straight-line length (end-to-end) through porous media (Fig. 3.12).

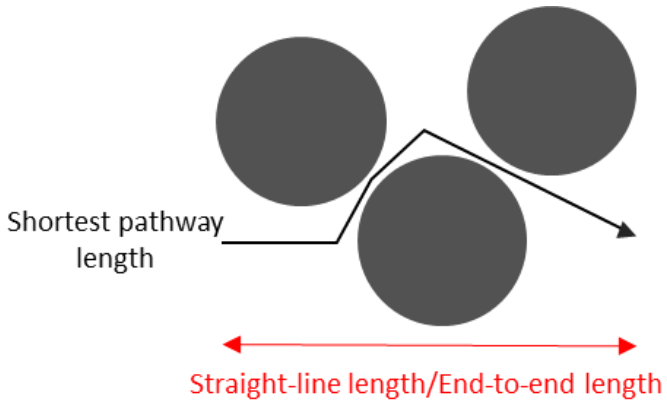

Figure 3.12. Geometrical tortuosity is calculated as the ratio of the shortest pathway length to the straight-line (end-to-end) length.

Thus, for the geometrical tortuosity calculations, the actual shape of the fluid particle trajectory is not being considered. In comparison, for example, for hydraulic (flow) tortuosity, the main consideration is that there are several possible pathways – streamlines – taken by fluid particles between 2 points which do not necessarily form a straight line and can get curved, especially, when the pore space gets constricted or expanded along the way (Fig. 3.13). Each of these streamlines has the travel time associated with it. The ratio of time-weighted average streamline length to the straight-line length is defined as hydraulic tortuosity. Electrical tortuosity is determined in an analogical way (Clennel 1997).

Thus, flow and electrical tortuosities do not necessarily equal to geometrical tortuosity. This is particularly true for pore networks with complex topologies. For more information about various types of tortuosity, refer to the paper by Clennel (1997). In our model, we use a Random Walk algorithm to calculate electrical and flow tortuosity.

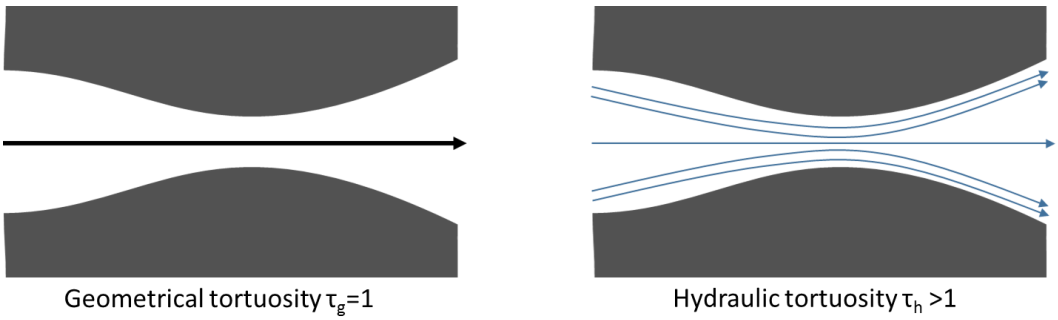

Figure 3.13. Illustration of the difference between geometrical and hydraulic tortuosity. For the same porous media, the left picture depicts the shortest pathway length used for geometrical tortuosity calculation, the right picture shows converging-diverging streamlines that are considered for hydraulic tortuosity calculation.

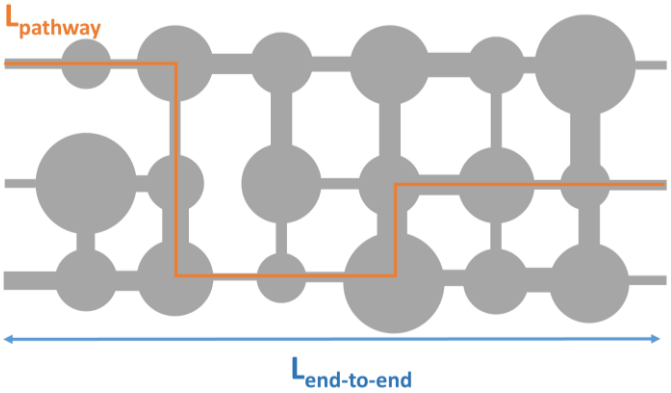

Figure 3.14. An example of one of the pathway lengths and end-to-end length for a pore network (Hakimov et al. 2018). Reprinted by permission of Copyright SPE.

Here our random walk algorithm is explained. We define a flow route as a chain of connected pores and throats spanning the whole network from inlet to outlet. For a volume of fluid/electron to be transported from inlet to outlet, it should pass through one of the available routes. One should note that different routes account for different percentages of the total flow which depends on the route's conductivity. In other words, some of the routes are more popular than the others depending on the routes' lengths, fluid

occupancies, and sizes of the constituent pores and throats. It is computationally infeasible to identify all possible pathways and calculate percentages of the total flow for each of them. Therefore, it is rational to calculate the average length of many particles traversing from inlet to outlet. To obtain reliable results, the number of particles should be high enough depending on the topology and connectivity of the pore network. A Random Walk algorithm is developed to simulate the movement of each particle. Initially, all particles enter the network from the inlet side. Giving more chances to throats with higher flow rates, each particle is then randomly assigned to an inlet throat. The particle then moves to the pore connected to the given inlet throat. Further, the particle can travel to any neighboring connected pore(s) that has lower pressure (or electric potential) than that of the current pore. If there is more than one option, the particle's trajectory is randomly chosen based on the throats' flow rates (or electric currents) that are connecting various destination pores. Once the particle reaches the outlet, the transversed trajectory is calculated. Repeating such calculations for many particles, the average pathway length is calculated. Tortuosity is then determined as the ratio of the average pathway length to the straight line (end-to-end) length of the network. (Fig. 3.14).

Chapter 4. Results

4.1. 2D pore-networks with introduced microporosity. Sensitivity of resistivity index and tortuosity to increasing microporosity.

As explained, we first generate 2D lattice macro-pore networks. Then, some of the macropores and/or throats are removed to create base pore networks. These networks are modified further by inserting micro-networks to include microporosity (denoted as networks B, C, D, and E in this section). Our generated pore networks can be divided into 5 different categories depending on the orientation of the removed throats and inserted micro networks (Fig. A-7). For each base pore network, several modified networks were generated. Fig. A-7 shows an example of the modified network for each group and their corresponding base networks. Thus, 5 different groups of simulations are designed in this section (Fig. 4.1). See Fig. A-8 in Appendices for a summary of all generated networks.

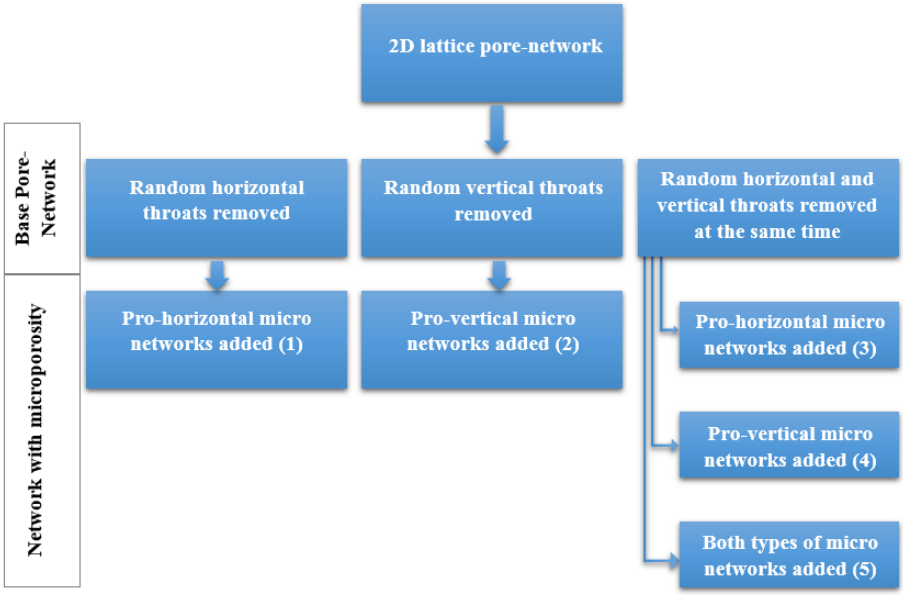

Figure 4.1. Five different groups of pore networks with microporosity used in this study (Hakimov et al. 2018). Reprinted by permission of Copyright SPE.

In the first group, the base pore network (A1) is created by removing random horizontal macro throats from lattice pore network. The inlet and outlet throats are located on the left and right sides of the network, respectively. Thus, removing horizontal throats results in significantly higher tortuosity (Fig. A-8). All the subsequent pore networks with microporosity (i.e., B, C, D, and E) are formed from the same base pore network by inserting pro-horizontal micro-networks. These networks have different percentages of the microporosity (i.e., 1.67% in network B, 3.97% for C, 7.26% for D, and 8.32% for E). This is done by increasing the number of inserted micro-networks into the base network, which are created by the random network generation algorithm and, therefore, can have a different number of pores/throats, pore sizes, pore volumes and etc.

All generated networks of this group (i.e., A1, B, C, D, and E) are then used for the simulation of drainage and imbibition processes. The sequences of flow simulations and their associated pore-level displacements are explained in the previous section. We calculate water saturation and electrical resistance at each quasi-steady state point during simulations. The results are shown in Fig. 4.2 indicating a significant decrease in the electrical resistance due to the existence of microporosity. In the presence of micro-networks, water pathways are shorter and consequently, the electrical resistance is lower during drainage and imbibition. This group illustrates in-series microporosity by resembling intragrain or intraparticle microporosity in rock samples. The results are plotted using a semi-log plot to specifically highlight the impact of microporosity on electrical resistance. It is also worth mentioning that the residual water saturation at the end of drainage is higher in networks with higher microporosity (Sirw in E > D > C > B > A1). This is because we don’t allow any oil-to-water displacement in the microporosity

regions. Drainage simulations are stopped when there is no valid displacement left in the macro-network. This causes all base networks of B, C, D, and E to have similar pore fluid occupancies at the beginning of imbibition. This is expected since we do not have any trapped water because of the oil-to-water displacements during drainage. All pores and throats have angular cross sections allowing water to remain in corners after oil invasion. We then inject water from the inlet to simulate imbibition where oil can get trapped due to piston-like and snap-off displacements. Since the water phase is connected throughout the network, snap-off displacements can occur in all oil-invaded elements. Imbibition is terminated once we reach residual oil saturation where the oil phase is completely disconnected from the outlet. We calculate electrical resistance and other flow-related properties during drainage and imbibition.

In the second group of simulations, the base pore network (A2) is created with a small tortuosity value (Fig. A-8). This value does not change much by inserting pro-vertical micro-networks (Fig. 4.3). Here, we investigate the effect of the microporosity that do not alter the shortest pathway from the inlet to outlet. As a result, Fig. 4.3 shows similar electrical resistance for the networks with different microporosity values.

The third, fourth, and fifth groups of simulations (Figs. 4.4, 4.5 and 4.6) have the same base pore network (A3), which is derived from the original lattice pore network by removing both horizontal and vertical macro throats. Pro-horizontal and pro-vertical micro-networks are inserted in groups 3 and 4, respectively. Group 5 has both types of inserted micro-networks (see Fig. A-7).

Groups 3 and 1 have similar results. The only difference is that electrical resistance curves do not shift down as much in group 3. This is caused by lower tortuosity of base network A3. Similarly, groups 4 and 2 have similar trends. Once again, the introduced pro-vertical micro-networks have only a volumetrical effect on the results and do not provide new shorter pathways for the electrical current from the inlet to the outlet and consequently, have no significant effect on the electrical tortuosity or resistance. Group 5 however, shows an observable downshift of the resistance curves for networks with higher microporosity values. In this group, adding micro-networks slightly decreases the electrical tortuosity.

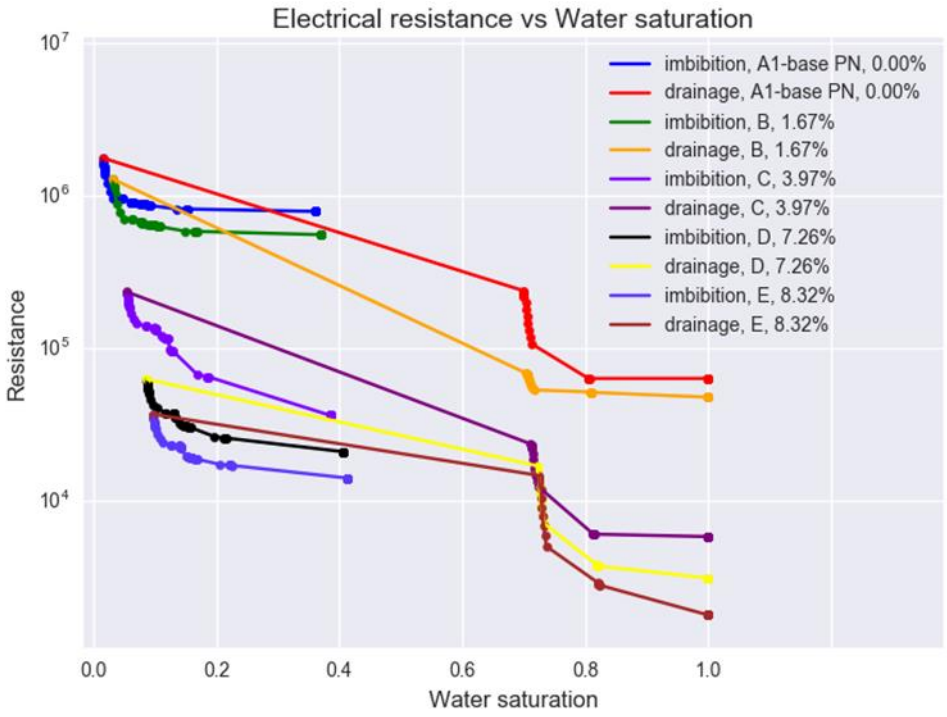

Figure 4.2. Electrical resistance versus water saturation during drainage and imbibition processes for the first group of generated networks where random horizontal macro-throats are replaced with micro-networks (Hakimov et al. 2018). Reprinted by permission of Copyright SPE.

The observed downshift of the resistivity curve is primarily caused by pro-horizontal micro-networks creating shortcuts for the electrical current (i.e., lowering electrical resistances).

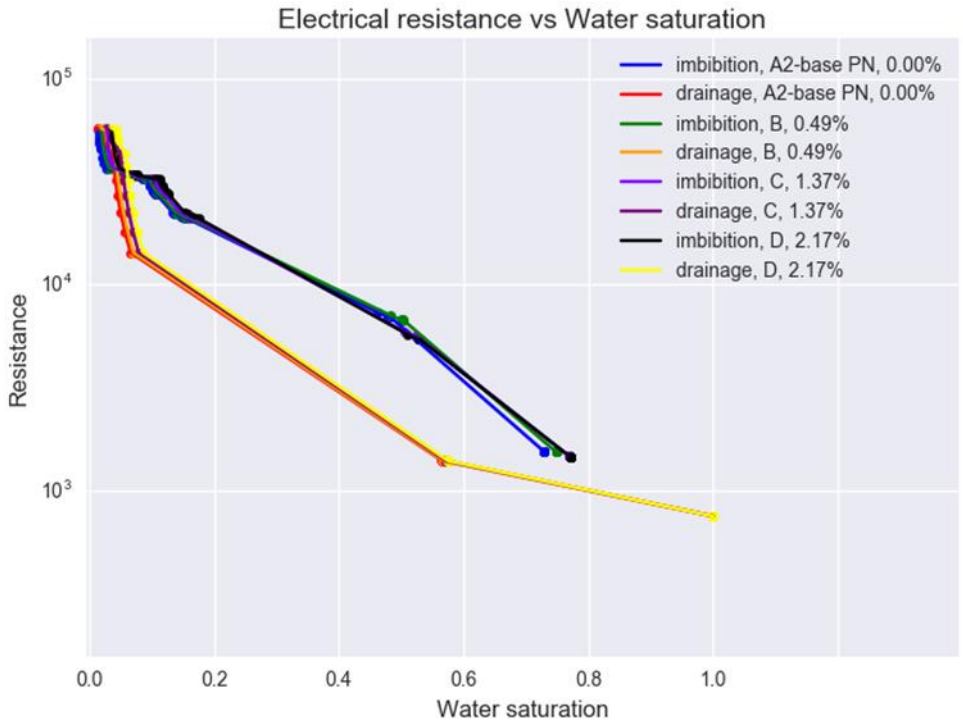

Figure 4.3. Electrical resistance versus water saturation during drainage and imbibition processes for the second group of generated networks where random vertical macro-throats are replaced with micro-networks (Hakimov et al. 2018). Reprinted by permission of Copyright SPE.

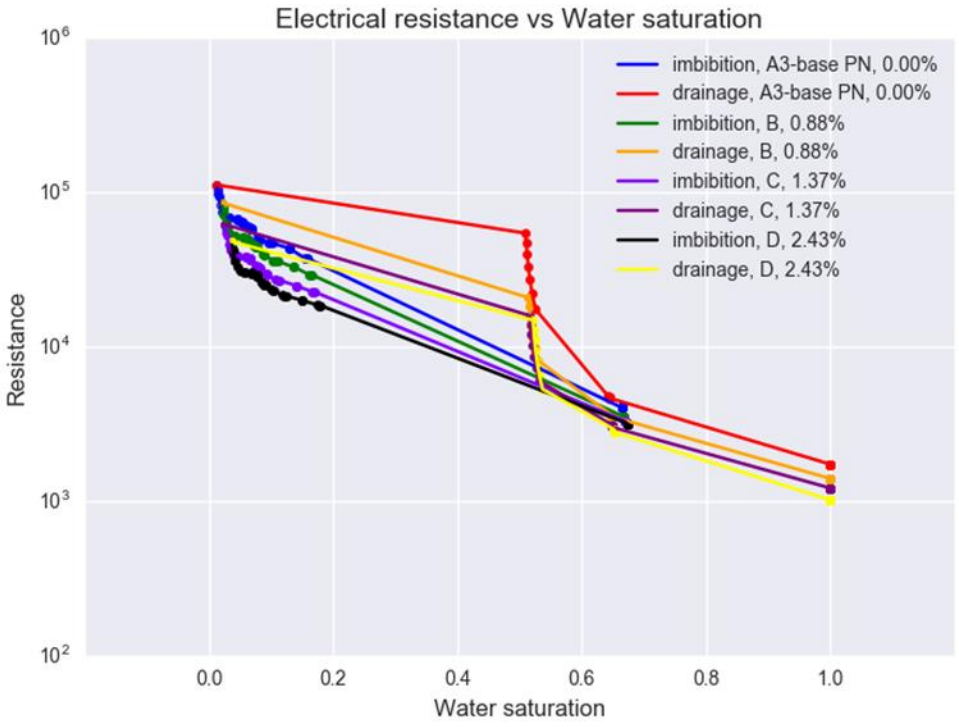

Figure 4.4. Electrical resistance versus water saturation during drainage and imbibition processes for the third group of generated networks where random vertical macro-throats are removed, and random horizontal macro-throats are replaced with micro-networks (Hakimov et al. 2018). Reprinted by permission of Copyright SPE.

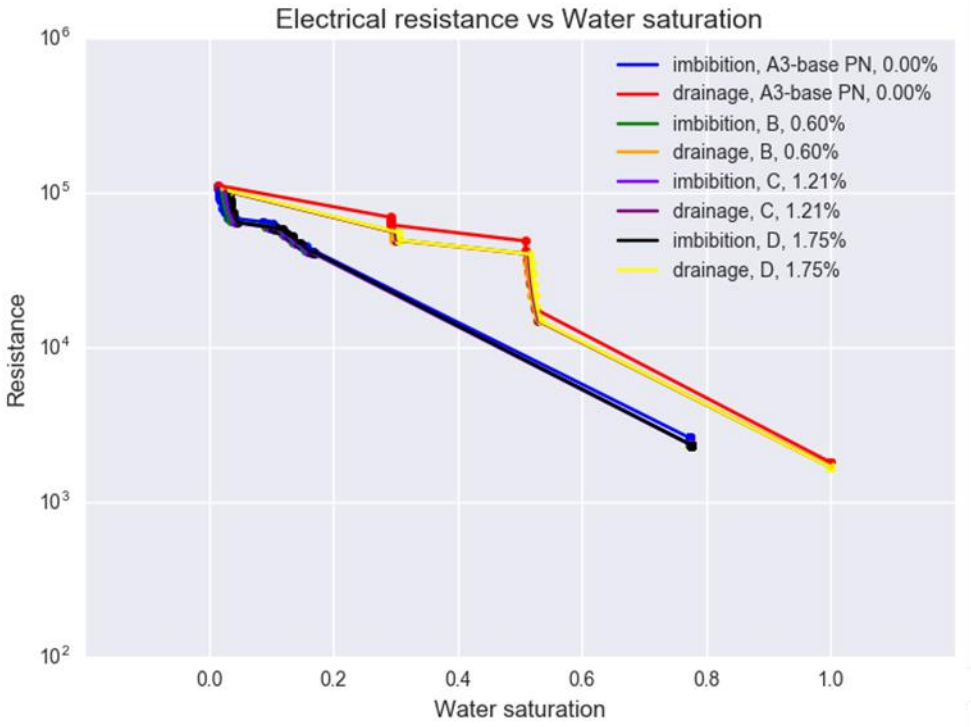

Figure 4.5. Electrical resistance versus water saturation during drainage and imbibition processes for the forth group of generated networks where random horizontal macro-throats are removed, and random vertical macro-throats are replaced with micro-networks (Hakimov et al. 2018). Reprinted by permission of Copyright SPE.

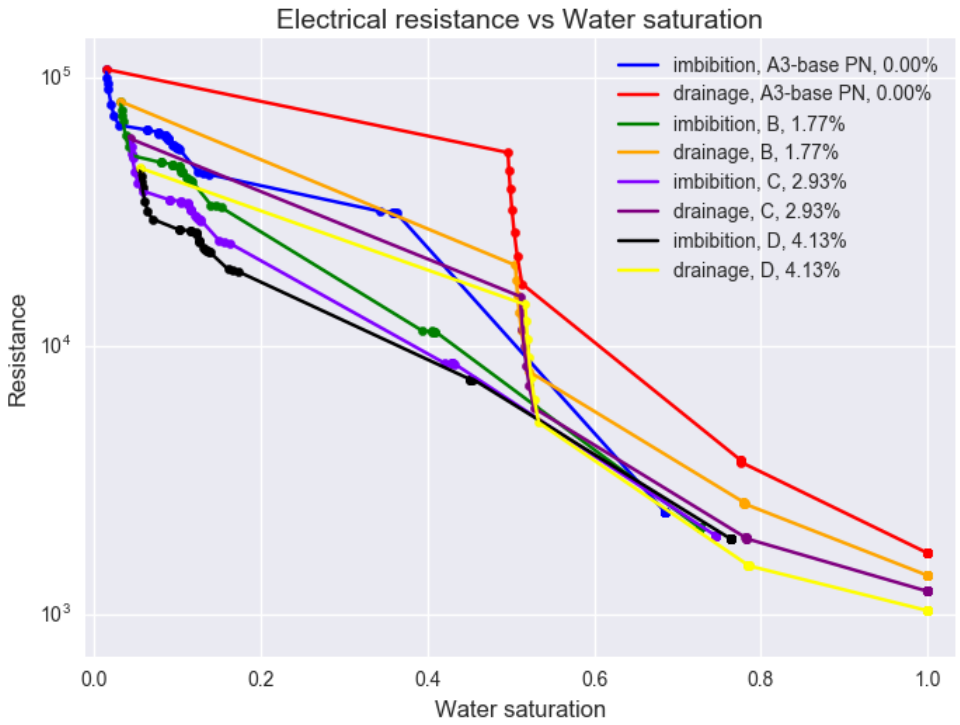

Figure 4.6. Electrical resistance versus water saturation during drainage and imbibition processes for the fifth group of generated networks where both random vertical and horizontal macro-throats are replaced with micro-networks (Hakimov et al. 2018). Reprinted by permission of Copyright SPE.

4.2. 3D pore networks. Effect of wide pore size distribution on the electrical properties

Here, we use two different 3D networks of Estaillades limestone and Berea sandstone to calculate electrical resistivity indexes. Berea sandstone is more homogenous compared to Estaillades limestone. First, we demonstrate the Archie equation's limits to estimate water saturation in the sample with wider pore size distribution.

4.2.1. Archie's calculated water saturation

The Archie equation (Archie 1942) is used to estimate water saturation in the more heterogeneous network of this work, i.e., Estaillades limestone. The results are compared with the actual water saturation from pore network modeling. At each quasi-steady-state step during flow simulations, we calculate water saturation and resistivity index as described in the previous section. Using the Archie equation, saturation can then be estimated for a given resistivity index as

$$S_w = (\frac{1}{IR})^{\frac{1}{n}} \qquad (16)$$

where IR and n are resistivity index and saturation exponent, respectively. We assume n=2 in this work.

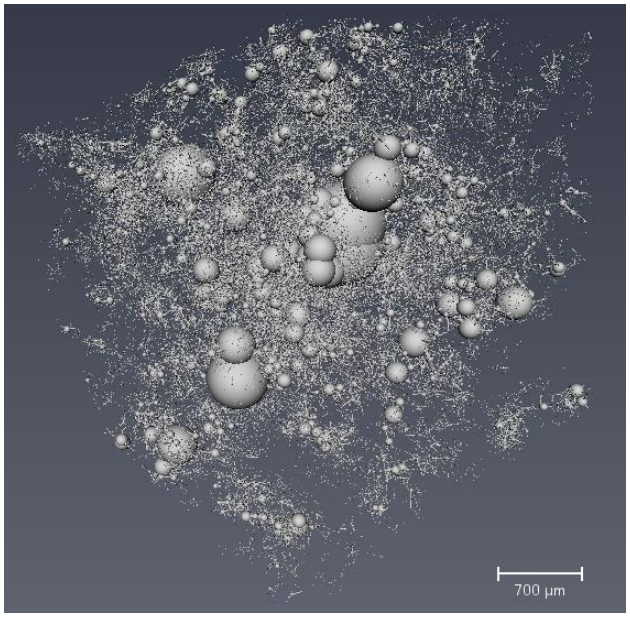

Figure 4.7. The pore network of Estaillades limestone generated from 3D CT-scan image of a dry sample. Note: some of the pores or throats are not clearly visible due to their small radii.

We used 3D CT-scan image of Estaillades limestone with 3.1-µm resolution (Bultreys et al. 2016) to extract the representative pore network. To do so, the Thermo Fisher Scientific™ PerGeos™ software package is used to extract the pore space from images, perform connectivity analysis, skeletonization, and clustering, and finally assign geometric properties to all generated pores and throats. Fig. 4.7 shows the representative pore network of the entire image volume (i.e., a cube with the dimensions 3096.9 µm × 3096.9 µm × 3100 µm). This network has 126586 pores and 316192 throats which is too large for our flow simulation. Therefore, a small sub-volume of the original image is used to generate a pore network for the simulation of drainage and imbibition flow cycles. Similar to the 2D networks, we assign equilateral triangles for the cross section of all pores and throats. The resistivity index during drainage is plotted in Fig. 4.8. The results indicate that the Archie equation fairly predicts intermediate and high water saturation but overestimates lower water saturation regions.

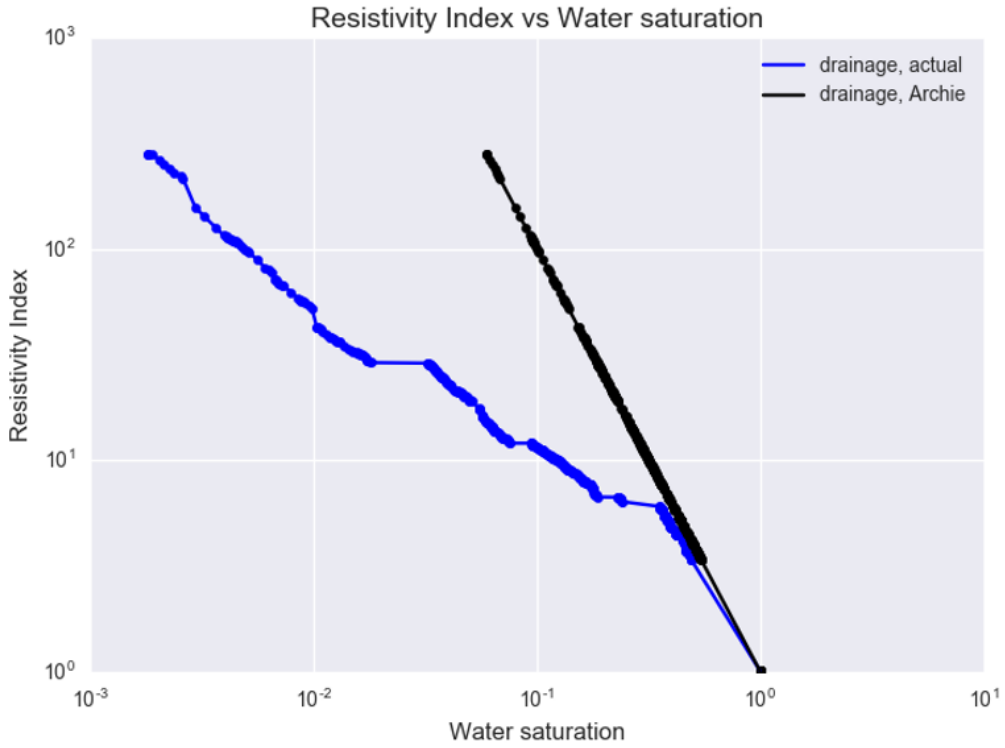

Figure 4.8. The comparison of Archie's calculated water saturation and actual water saturation from the PNM of Estaillades-1 sub-volume during primary drainage (Hakimov et al. 2018). Reprinted by permission of Copyright SPE.

4.2.2. Comparison to Berea sandstone

To illustrate the effect of wide pore size distribution further, we compare electrical resistivity of Estaillades to that of more homogeneous Berea sandstone sample. For Berea, we use the pore network of Oren at al. (1998) consisting of 12351 pores and 26147 throats (Fig. 4.9). The Estaillades pore network was generated using a larger sub-volume of the 3D images of Bultreys et al. (2016), i.e., Estaillades-2. It consists of 25718 pores and 45904 throats (see Fig. 4.10 and Fig. A-9 in the Appendices). Pore size distributions of both samples are shown in Fig. 4.11. Resistivity indices during drainage are plotted in Fig. 4.12. Berea's curve forms almost one single slope while Estaillades shows drastic

changes in the water saturation with different slopes along the way. The latter cannot be described with the Archie equation.

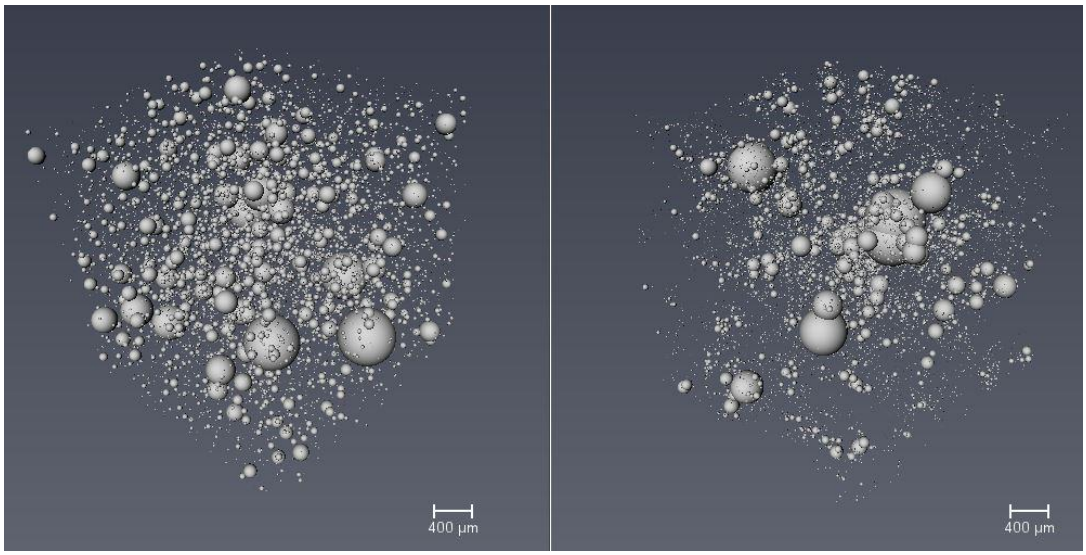

Figure 4.9. Pore networks of the Berea sandstone on the left and Estaillades limestone on the right. Note: throats are hidden to make pores more visible. Sphere sizes represent each pore volume.

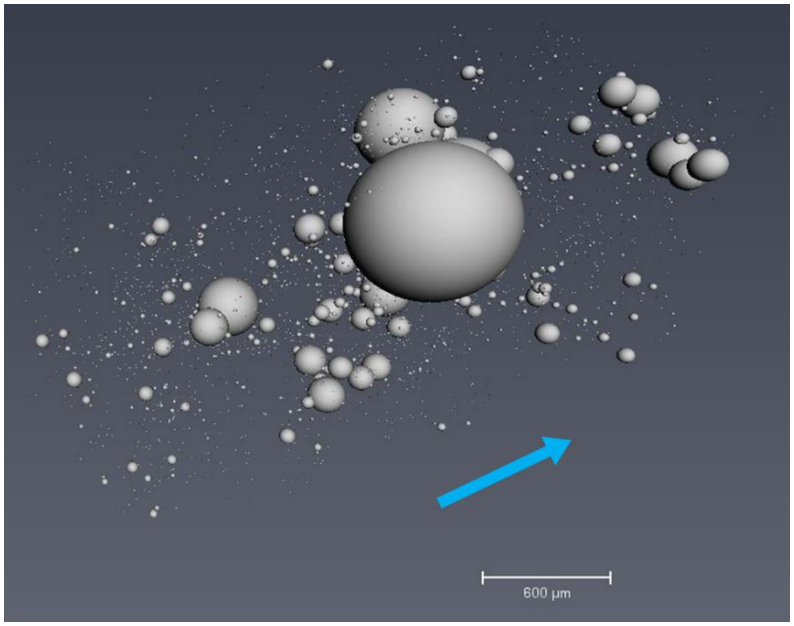

Figure 4.10. Pore Network of the Estaillades-2 sub-volume where the blue arrow shows the injection direction. Note: throats are hidden to make pores more visible.

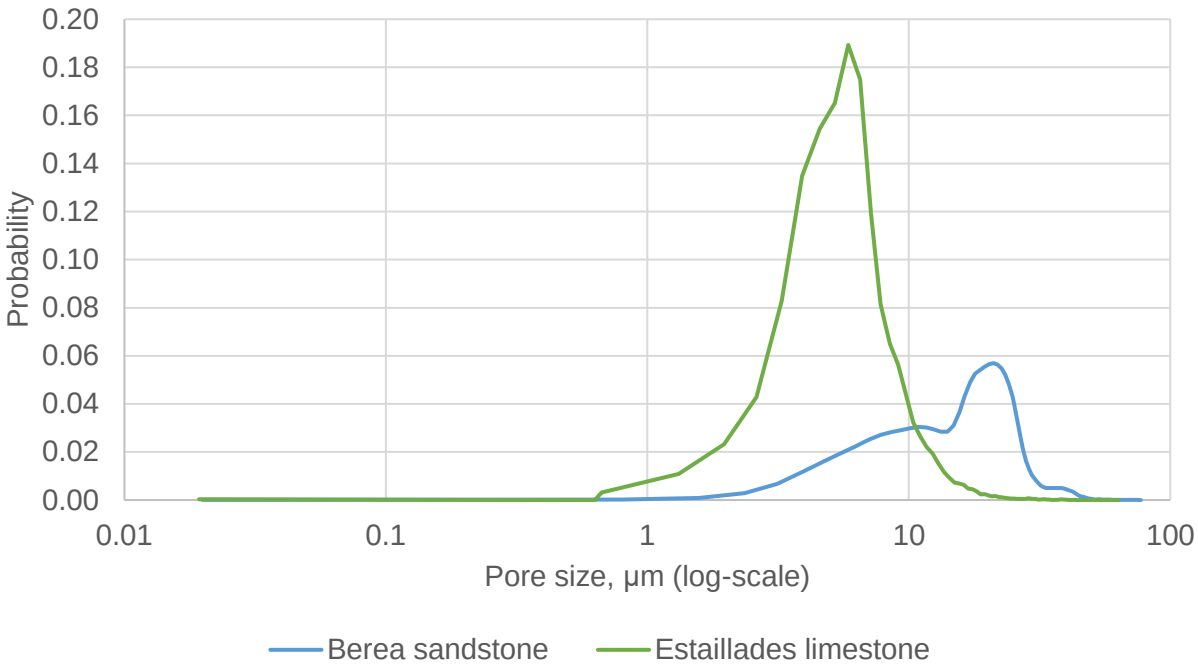

Figure 4.11. The comparison of pore size distributions for the Berea sandstone and Estaillades limestone.

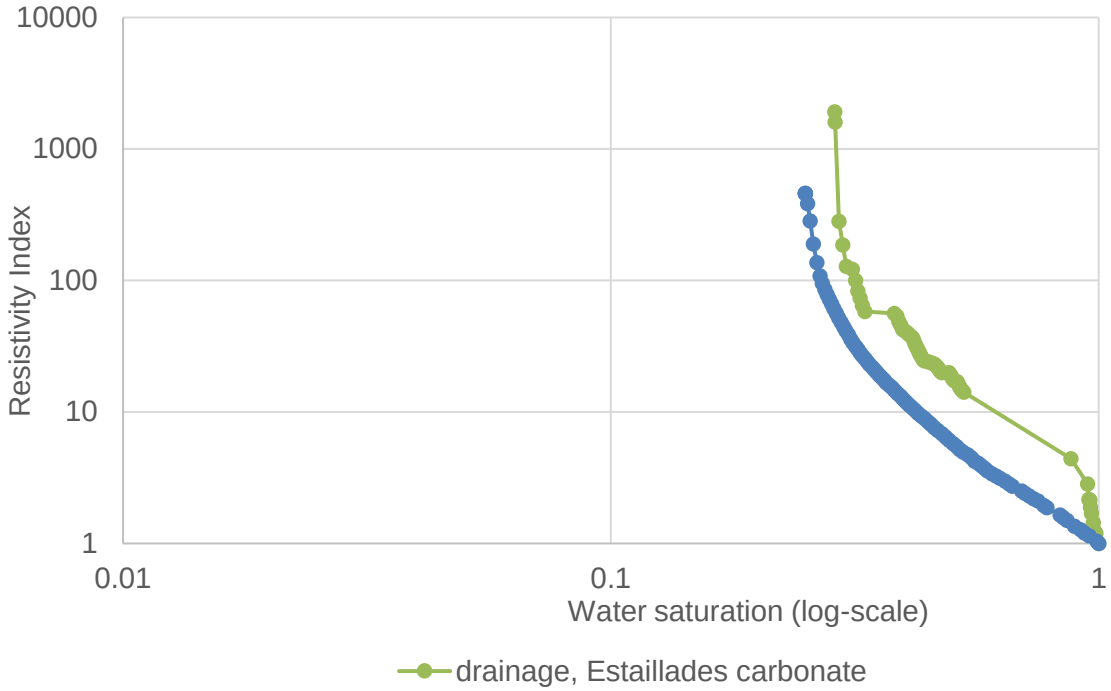

Figure 4.12. The electrical resistivity of the Berea sandstone and Estaillades limestone during primary drainage.

4.3. 3D pore-networks. Impact of microporosity related parameters on electrical and transport properties of the rock sample

In total, 15 pore-networks have been generated with five for each of three pore size distributions (small, medium and large) matching five different target local porosities in microporosity zones (10%, 20%, 30%, 40% and 50%). The summary with the properties of each network is provided in the table below (Table 4.1).

Two-scale pore-network	Number of pores	Number of throats	Total porosity	Micro PV / Total PV	Absolute permeability, md	Isolated porosity
S-10	30183	69828	6.83%	20.79%	0.446	0.02%
S-20	38173	89711	7.53%	28.14%	0.682	0.02%
S-30	42604	100096	7.43%	27.18%	1.126	0.03%
S-40	45684	107806	7.51%	27.96%	1.625	0.04%
S-50	47684	112745	7.56%	28.44%	1.836	0.04%
M-10	13675	20944	8.62%	37.27%	1.027	2.31%
M-20	14998	26124	9.26%	41.57%	1.797	1.53%
M-30	15799	28951	9.14%	40.81%	1.999	0.71%
M-40	16294	30731	9.25%	41.53%	3.142	0.55%
M-50	16705	31961	9.23%	41.39%	2.545	0.63%
L-10	12196	13385	14.46%	62.60%	0.004	7.12%
L-20	12465	14525	14.78%	63.40%	0.910	5.17%
L-30	12635	15246	14.98%	63.88%	0.998	4.03%
L-40	12731	15499	14.42%	62.49%	2.278	2.82%
L-50	12787	15682	14.67%	63.12%	0.967	5.11%

Table 4.1. Summary of the properties for the all generated pore networks.

As can be seen from the table (Table 4.1) and bar charts (Fig. 4.14, 4.15), increasing pore sizes not necessarily resulted in a higher permeability — this can be explained by the several factors related to the way that micro network generation algorithm works. First of all, for each microporosity cluster, micro pores are being generated until the target local porosity is matched. Pore sizes are being chosen randomly from the array that is generated in advance and matches the given pore-size distribution. Before being assigned to the micro pore, each randomly chosen pore radius is checked for 2 criteria:

1) It should geometrically fit the given microporosity cluster, i.e. not exceed dimensions of the given space occupied by microporosity (the pre-set relative tolerance should not be exceeded).
2) Adding the given pore radius should not result in the local porosity greater than the target value (similarly, the relative tolerance is checked).

If any of these conditions is not satisfied, the randomly chosen pore size will not be added to the network. In that case, another random choice will be made. In case there is no pore size in the pre-generated pore-size distribution that would match these criteria, no pore will be created.

Therefore, depending on the available pore size options and how close the current local porosity (after creating some number of micro pores) is to the target value, a pore might be generated or not generated at all. This means that in the same cross-section of the sample's cubic domain there might be less pore area open to flow in the L-networks than in the S-networks. In case with the large pore size distribution (the same as with the medium distribution in comparison with the small one), execution of the algorithm results in generating fewer number of pores leading to a smaller area open to the flow. However, this is not the sole contributor leading to these results. The second important factor is poorer pore connectivity of the L-networks in comparison with the S-networks. As can be seen from the graph (Fig. 4.13), L-10 has significantly higher number of pores with the coordination number of 1, while S-10 has the mean coordination number of 5. In other words, there are higher number of 'dead-end' or 'cul-de-sac' pores in L-10 than in S-10.

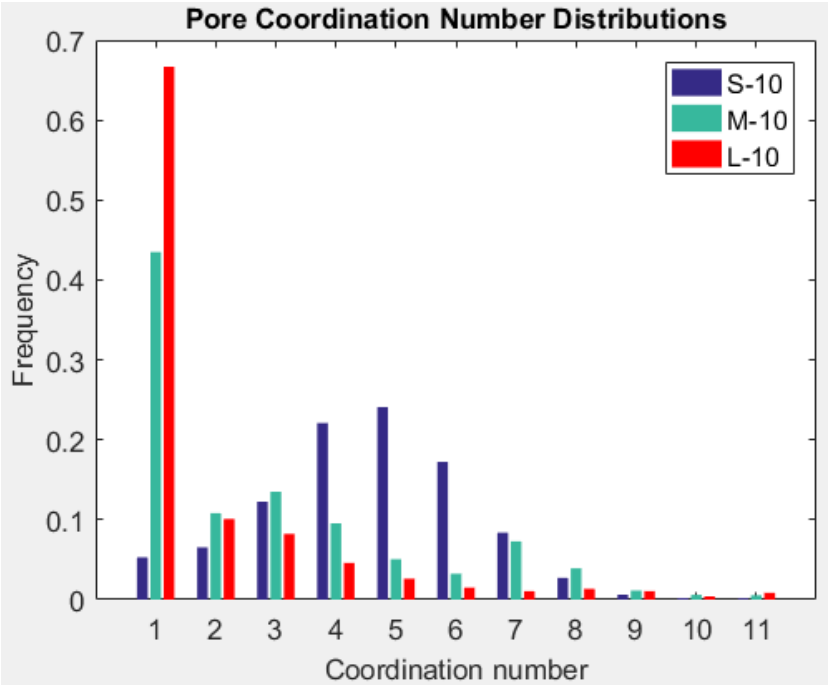

Figure 4.13. Comparison of the pore coordination number distributions for stochastically generated networks: S-10 (with small-sized micro pores), M-10 (with medium-sized micro pores) and L-10 (with large-sized micro pores). Note: bars for coordination numbers higher than 11 are not shown because of very low frequency for all three networks.

Generally, choosing the right pore size distribution and porosity for micro pore-network(s) that would populate microporosity zone(s) can be very challenging, since a set of some given pore size distribution and porosity might perfectly fit some microporosity clusters and might not fit the others. Therefore, the questions of geometrical and volumetrical compatibility (suitability) of the chosen input parameters with (for) the microporosity zones of the given sample are hard to answer beforehand, without the execution of the micro pore-network generation algorithm.

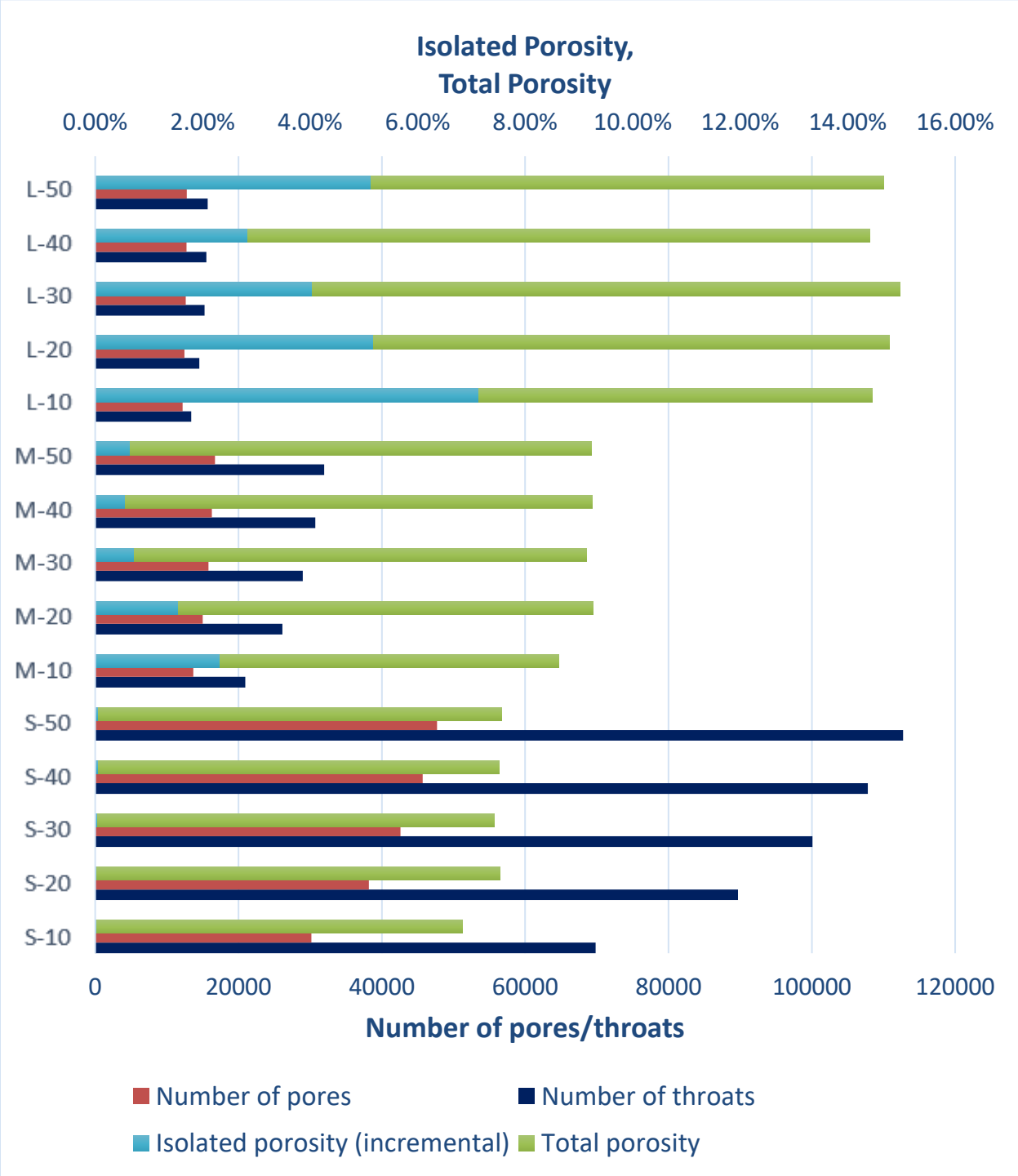

Figure 4.14. Bar chart with the comparison of the number of pores and throats, isolated and total porosity for all the generated networks.

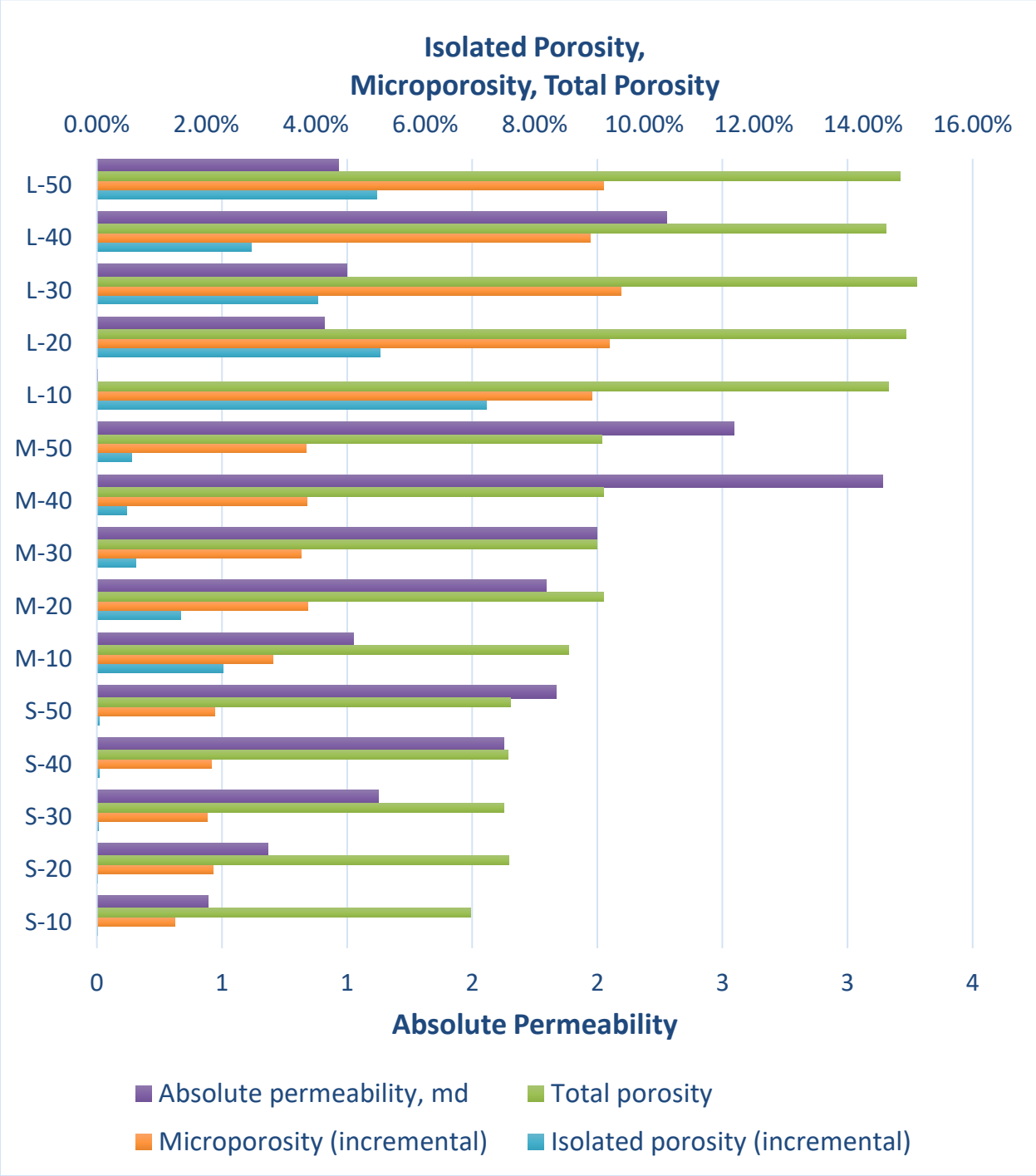

Figure 4.15. Bar chart with the comparison of the absolute permeability, incremental microporosity, isolated and total porosity for all the generated networks. Note: absolute permeability for L-10 is not visible on the graph due to very low value compared to permeability axis scale.

4.3.1. Capillary pressure results

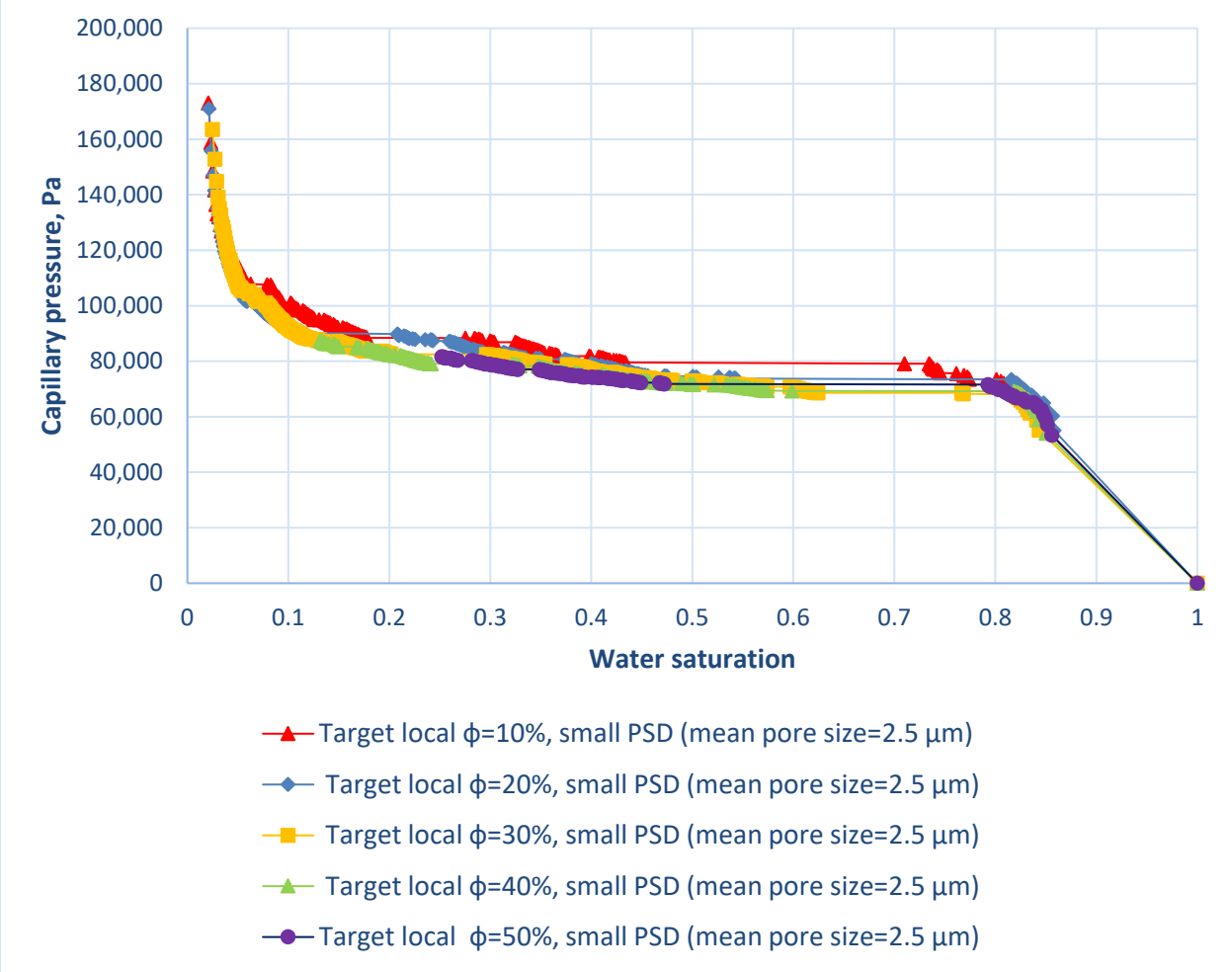

Figure 4.16. Capillary pressure curves during primary drainage generated for the pore-networks with small micro pores in microporosity zones.

Capillary pressure results for primary drainage simulation indicate that the curves generated for the five pore-networks with the small PSD almost coincide (Fig. 4.16). This demonstrates weak sensitivity of the capillary pressure to the local porosity of the microporosity zone at the given small pore size distribution for the given rock sample.

However, the porosity seems to come into play in networks with the larger micro pores (M- and L-networks). As an example, the curves generated for the M-networks stretch

further to the left as the porosity increases (see Fig. A-1, A-2). This can be explained by the fact that the networks with the bigger target local porosity have smaller isolated porosity and hence, lower trapped water saturation.

Fig. 4.17 shows all the generated capillary pressures generated for 15 pore-networks in one plot. It can be seen from the graph, smaller pore sizes, as could be expected, lead to higher capillary pressures.

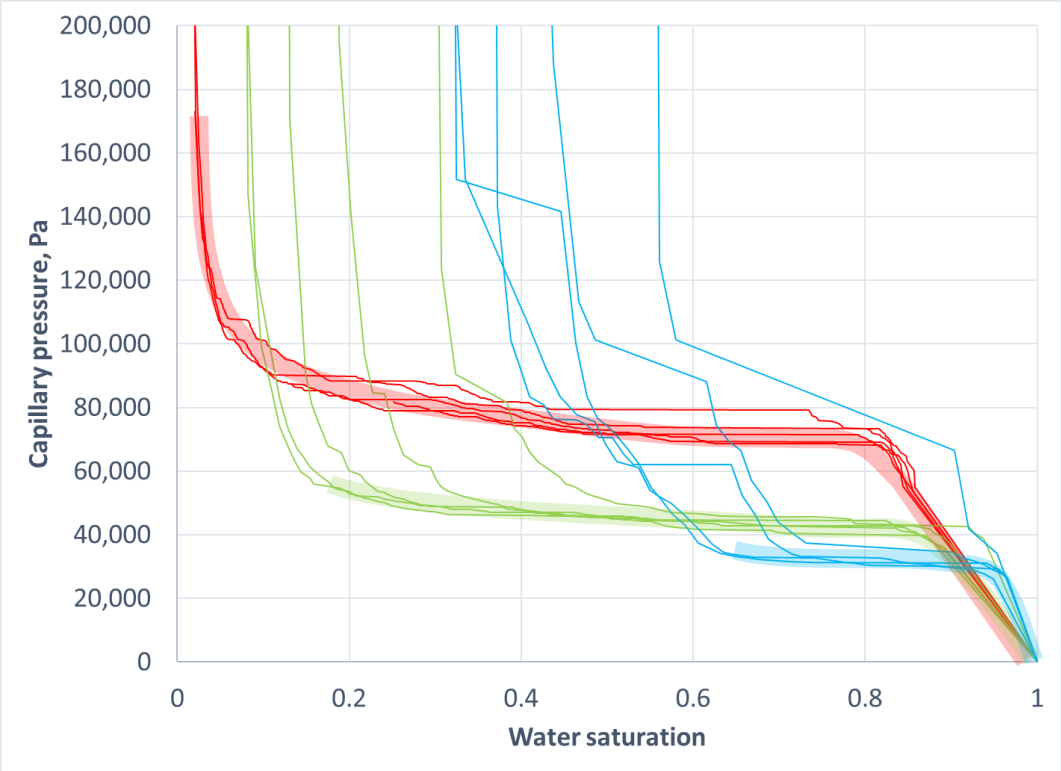

Figure 4.17. Capillary pressure curves during primary drainage generated for the all pore-networks. Red curves represent S-networks (small-sized micro pores), blue — M-networks (medium-sized micro pores) and green — L-networks (large-sized micro pores). Transparent areas are shown in order to group the results in separate clusters.

4.3.2. Relative permeability results

The relative permeability results for S-networks during primary drainage can be seen on Fig. 4.18. Similarly to capillary pressure results, all 5 curves overlap indicating weak sensitivity to the local porosity within microporosity zones. However, for the bigger pore sizes (M- and L-networks) with the different local porosities the curves become more spreaded although a clear trend with regard to local porosity cannot be established (Appendix B-1, B-2).

The big impact of pore size distribution on the results can be observed again when all the 15 cases are plotted in one figure (Fig. 4.19). General trend, as expected, is that increasing pore sizes, due to having smaller entry capillary pressures, speed up oil invasion and oil reaching to outlet — that is why oil relative permeability shoots up to high values in L-networks much earlier than that occurs in S- and M-networks (Fig. 4.20). At the same time, in the networks with the larger pores water relative permeability drops much faster than that happens in the other two groups of networks (S- and M-) because of oil already invading the majority of the pores right at the beginning of the drainage.

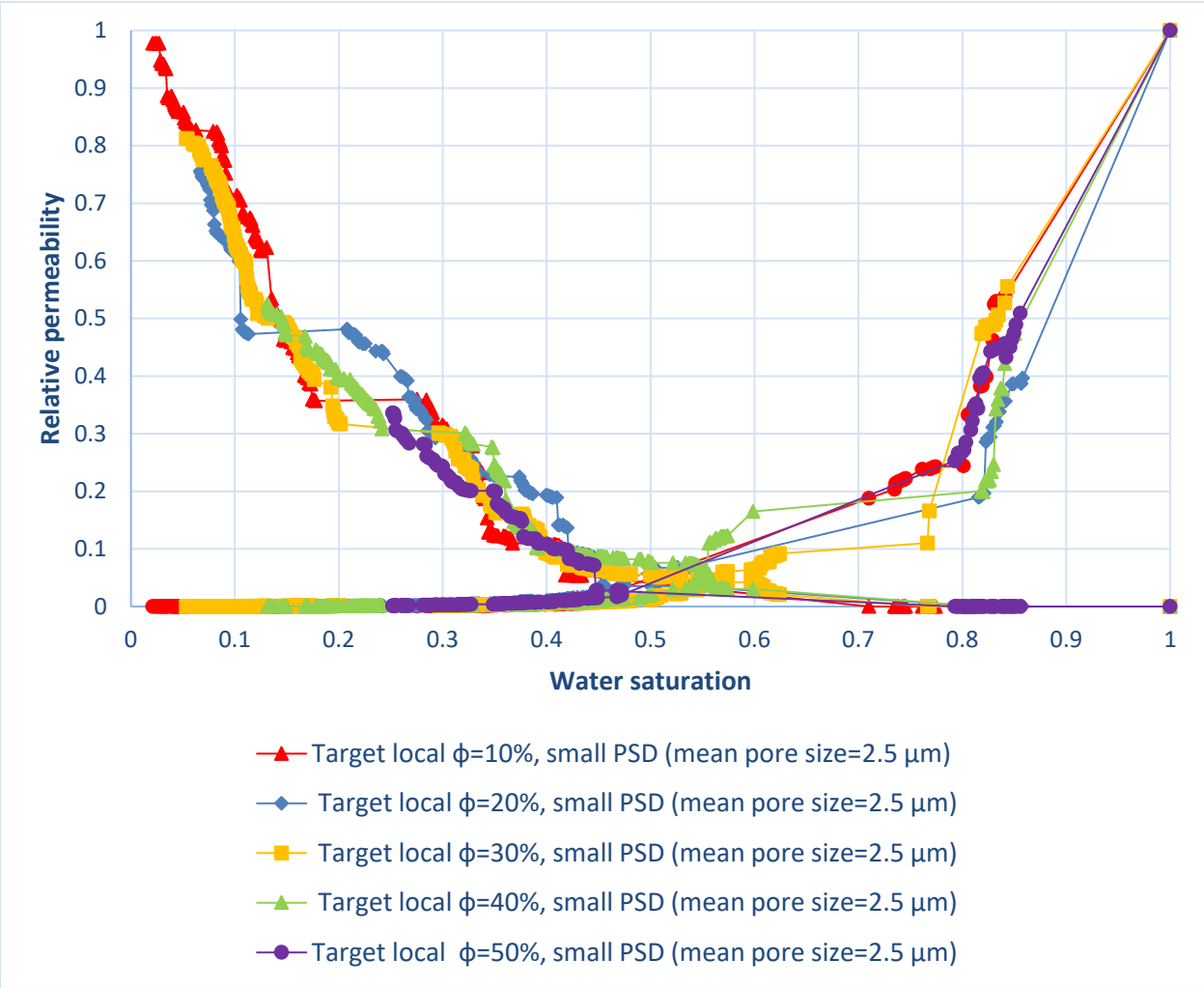

Figure 4.18. Relative permeability curves during primary drainage generated for the pore-networks with the small-sized micro pores in microporosity zones.

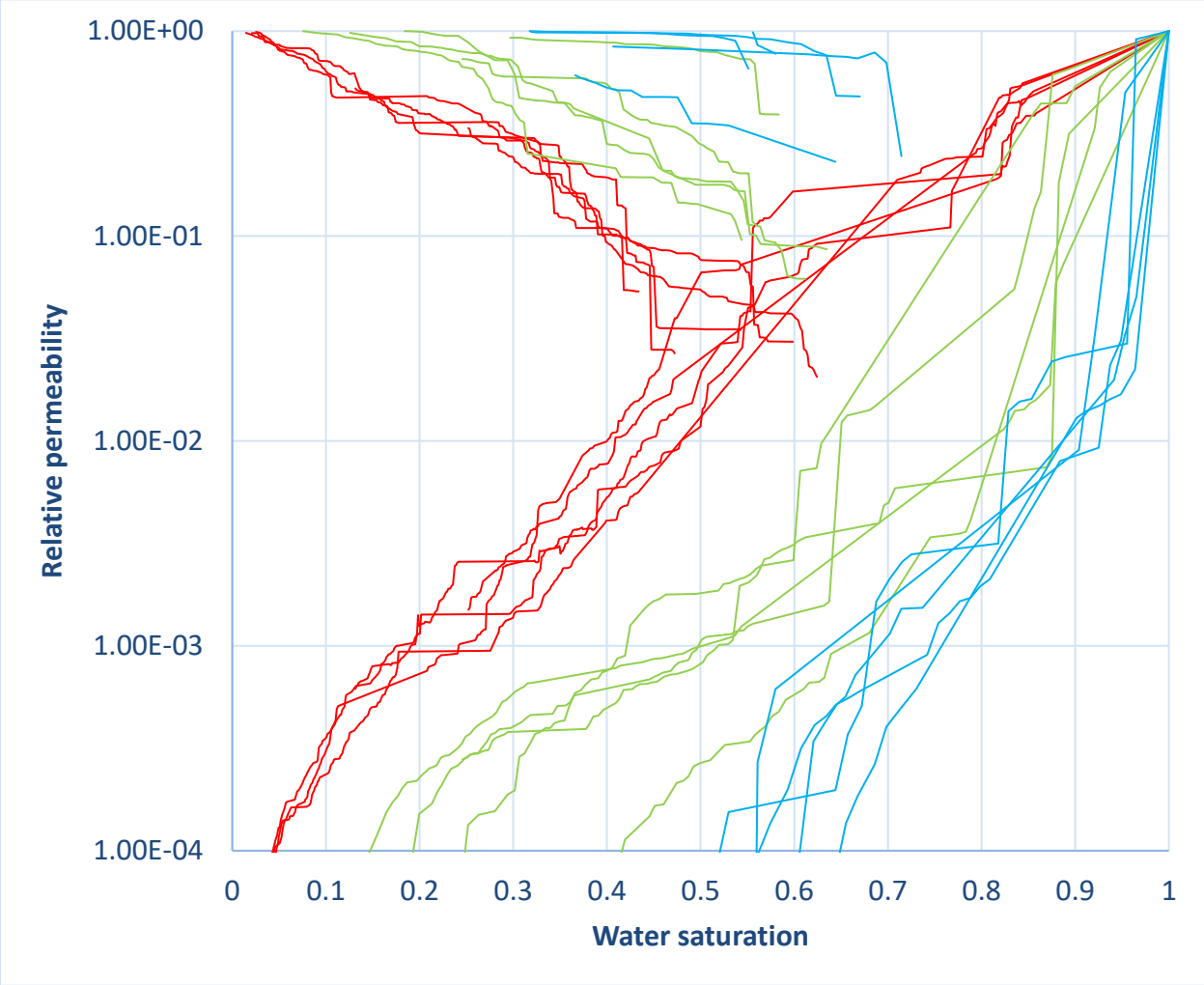

Figure 4.19. Relative permeability curves during primary drainage generated for the all pore-networks. Red curves represent S-networks (small-sized micro pores), blue — M-networks (medium-sized micro pores) and green — L-networks (large-sized micro pores). Relative permeability axis is shown in log-scale. For the purpose of more clear visualization, oil relative permeability curve is not connected all the way till zero value, i.e. only non-zero values of oil relative permeability are plotted and connected.

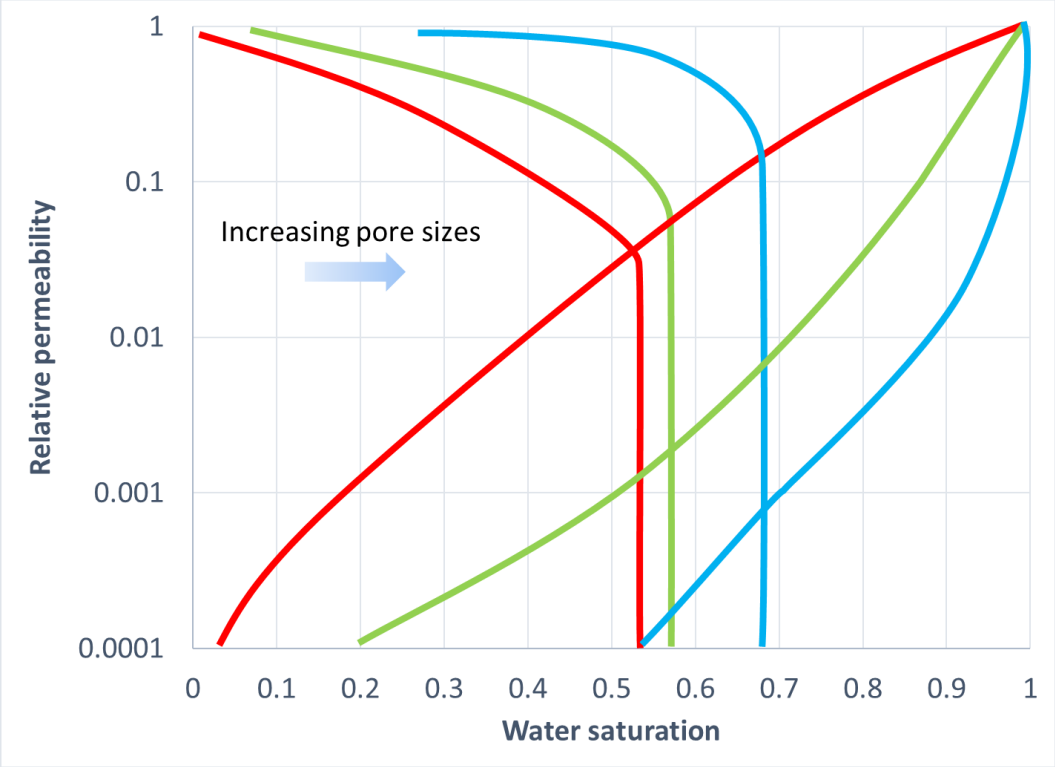

Figure 4.20. Approximate type curves determined based on the results for relative permeability during primary drainage for three groups of pore-networks. Red curve corresponds to the group of pore-networks with the small-sized pores in microporosity zone, green — to the group with the medium-sized micro pores and blue — to the group with the large-sized micro pores. Relative permeability axis is shown in log-scale.

4.3.3. Resistivity Index results

At each quasi-steady-state step during primary drainage simulation, water saturation and resistivity index have been calculated. Apart from the generated results, RI curve (the straight line on log-log scale) calculated based on the Archie equation (Eq. 11) is shown on the plot for the comparison. We assume the saturation exponent, n=2.0 for this set of simulations.

First, we present the results obtained for pore networks where microporous zones were populated with the pore-networks of small pore size distribution (Fig. 4.21).

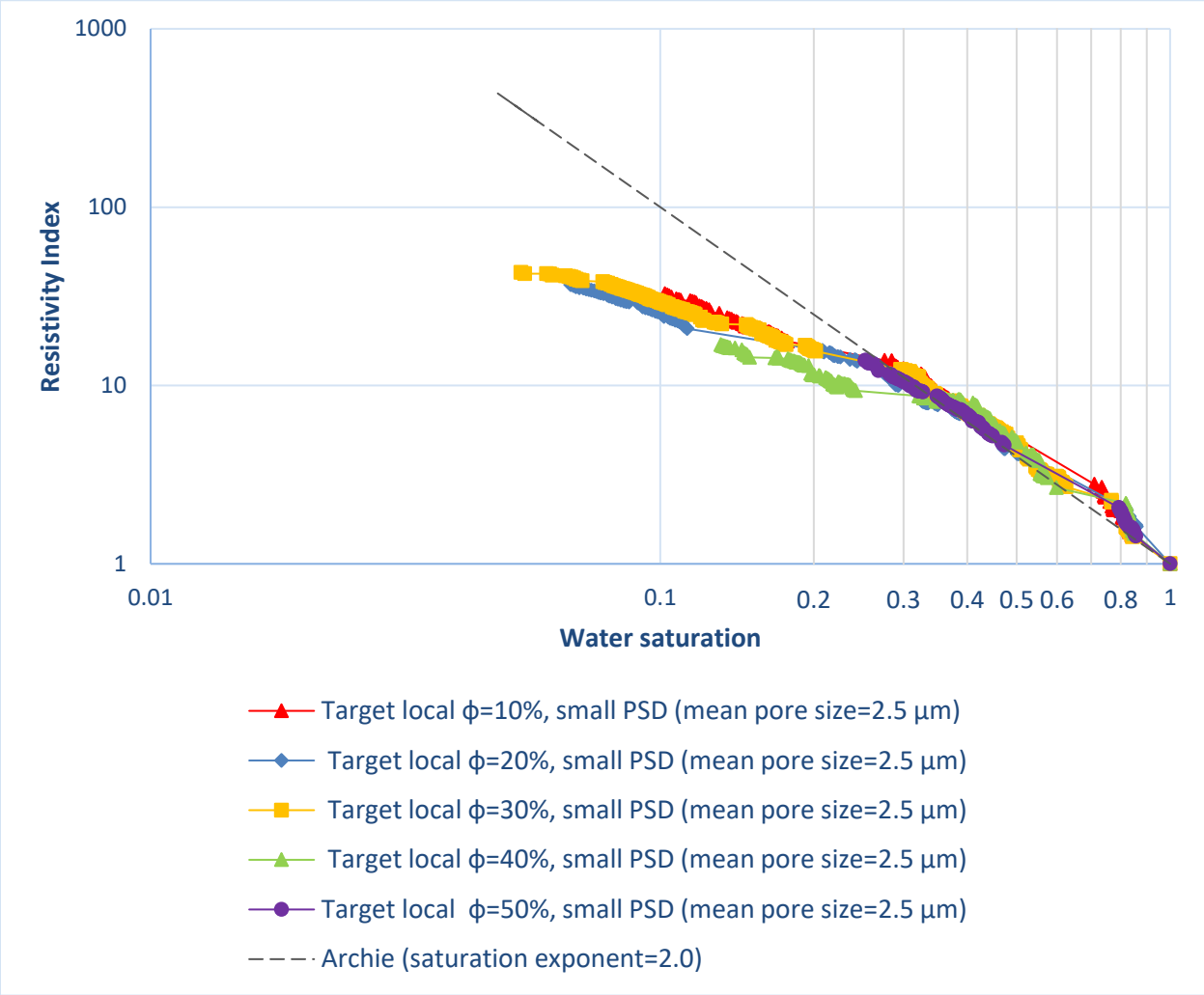

Figure 4.21. Resistivity Index curves during primary drainage generated for the pore-networks with small micro pores in microporosity zones. Both axes are shown in log-scale.

The plot shows that the local porosity in microporosity zone almost does not have any impact on the results, and all the five curves overlay each other. Besides, the results indicate a good match with the Archie equation at high and intermediate water

saturations, however, there is a deviation from the straight line at low saturation values. In other words, at some given Resistivity Index, Archie equation yields higher water saturation than the actual value is. Absolutely similar result has been generated for the electrical Resistivity Index during primary drainage simulation in Estaillades pore-network. This can be attributed to the fact that adding stochastic pore-network makes the resulting pore-network more heterogeneous. It can be better demonstrated by the comparison of all three types of the generated networks (S-, M-, L-) for some given porosity. The example provided below shows the pore size distributions comparison for three generated networks with the same target local porosity in microporosity zone (10%) but with the different pore sizes (small, medium and large) (Fig. 4.22, Fig. 4.23).

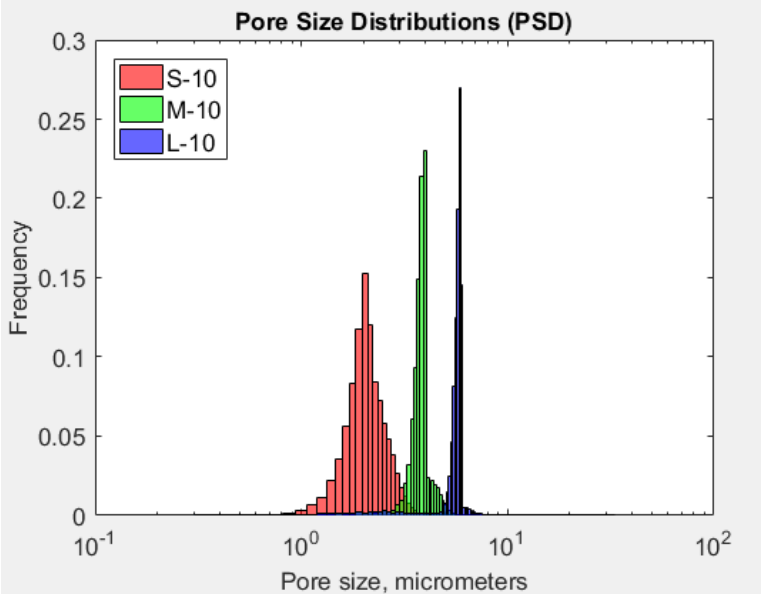

Figure 4.22. Pore Size Distribution comparison for three generated pore-networks (S-10, M-10, L-10) with the same local porosity (10%) but with the different micro pore sizes.

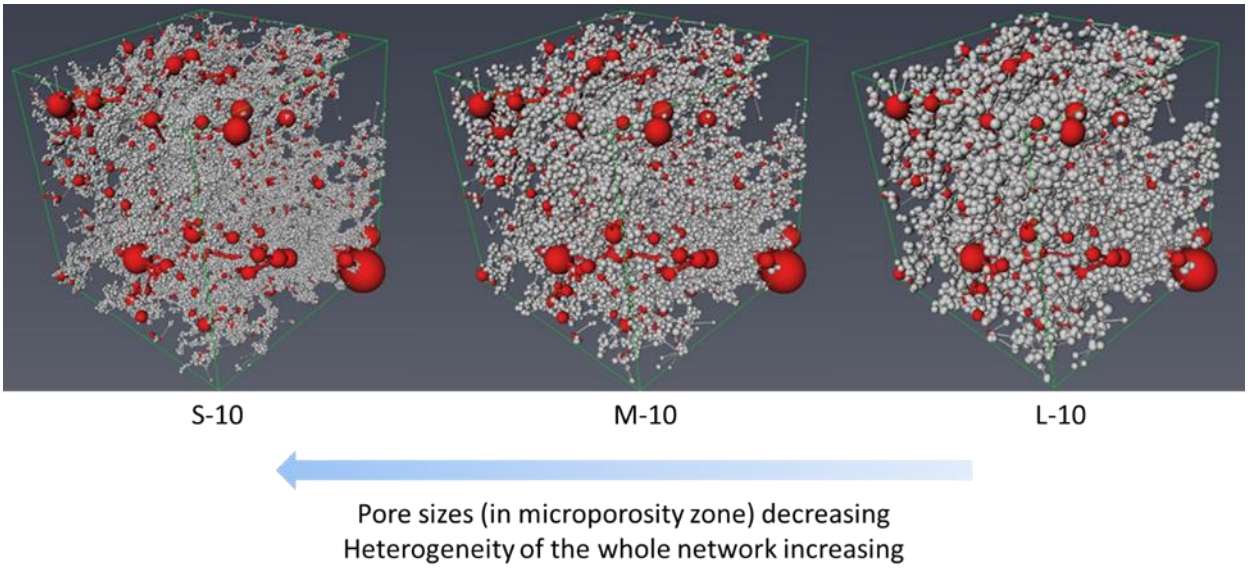

Figure 4.23. Visual comparison of three generated pore-networks (S-10, M-10, L-10) with the same local porosity (10%) but with the different micro pore sizes.

Comparing Resistivity Index curves generated for all 15 pore-networks in one plot (Fig. 4.24), one of the important effects that can be observed is the way pore size distribution impacts the Resistivity Index curve. Specifically, decreasing pore sizes in microporosity zones eventually causes the middle-drainage or late-drainage part of the curve to bend down forming an additional slope that can be attributed to the micro pores invasion by the oil.

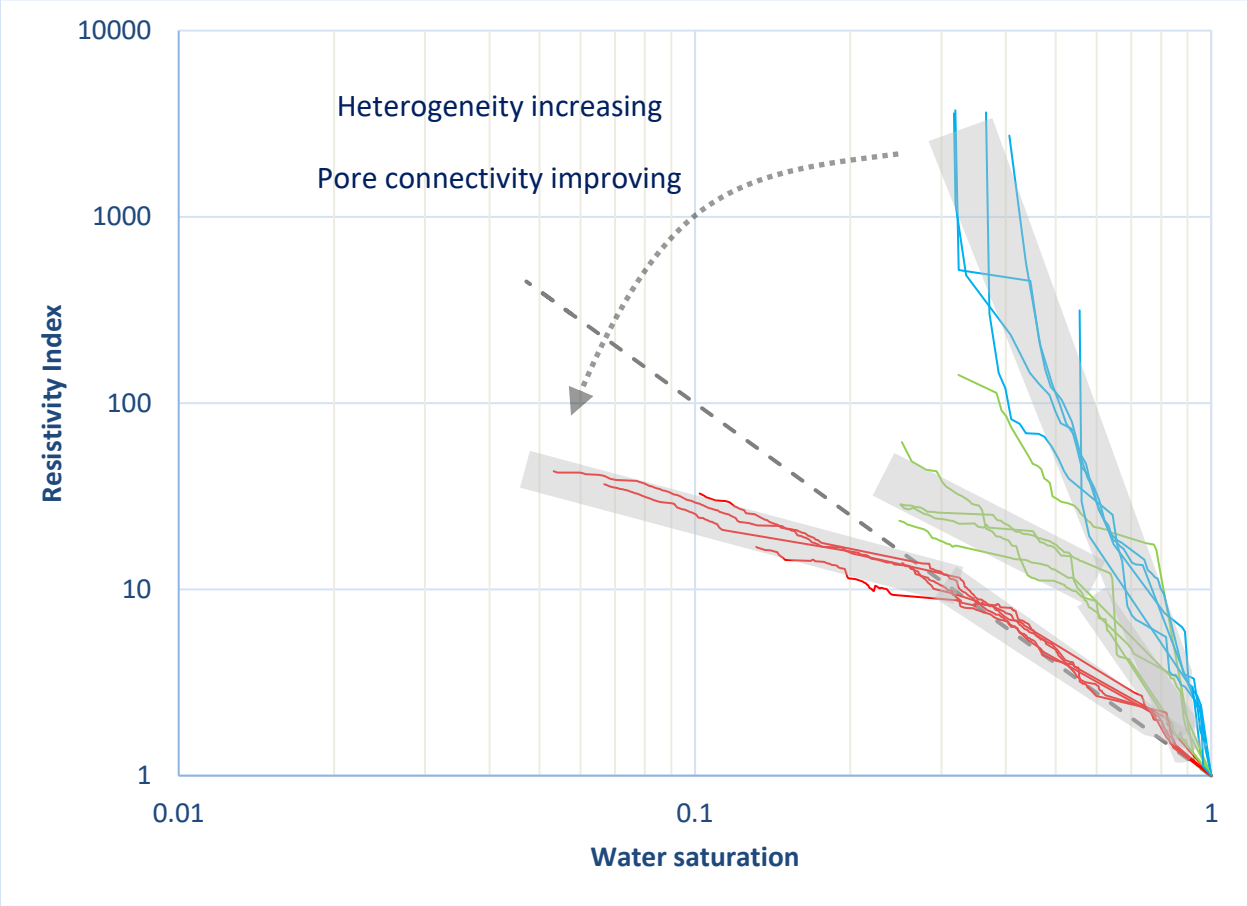

Figure 4.24. Resistivity Index curves during primary drainage generated for the all pore-networks. Red curves represent S-networks (small-sized micro pores), blue — M-networks (medium-sized micro pores) and green — L-networks (large-sized micro pores). Transparent grey areas are shown in order to group the results in one cluster.

4.3.4. Impact on reserves estimation

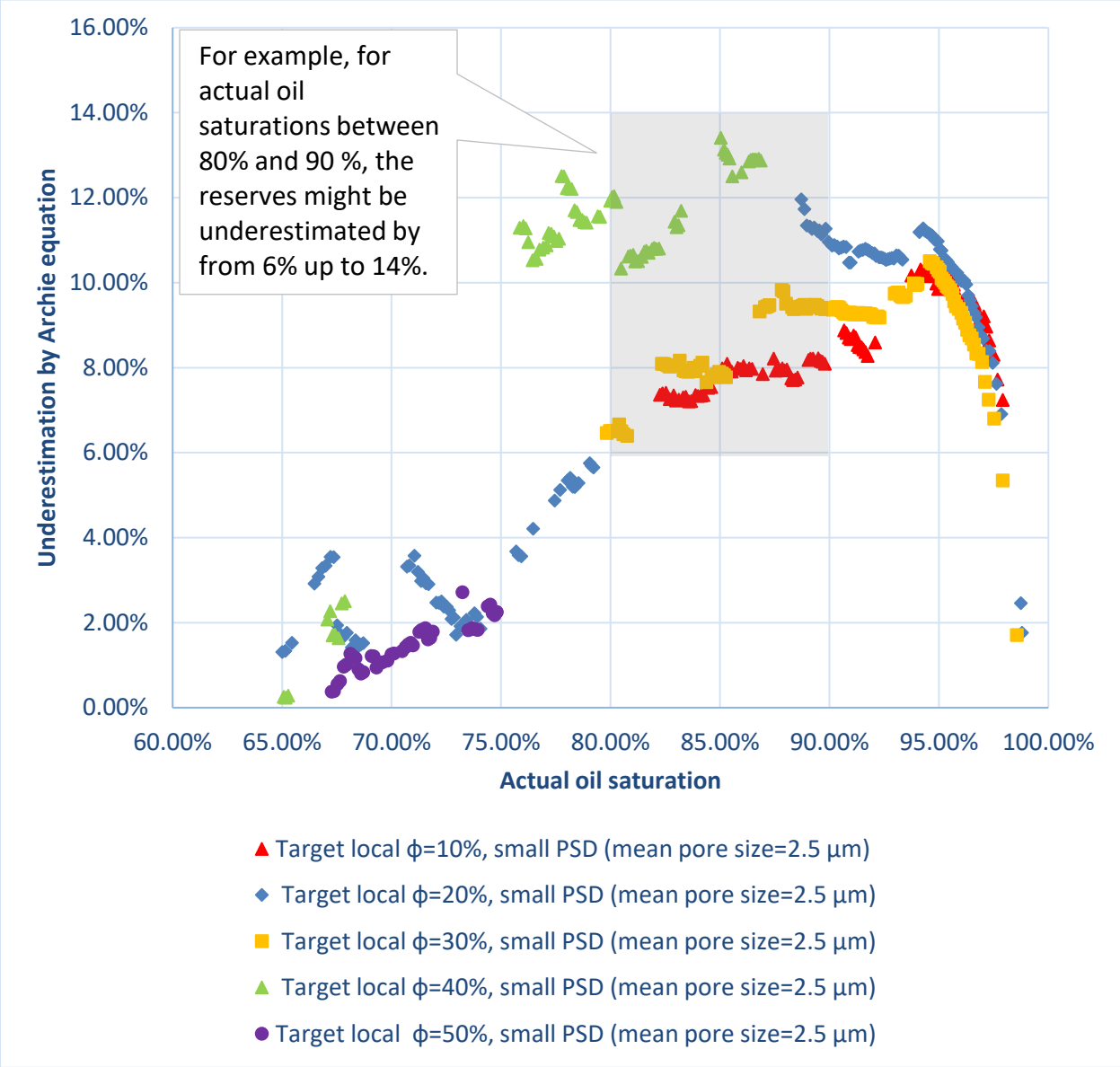

Figure 4.25. The plot shows by how much (%) the reserves estimated using Archie equation would differ from the actual value.

Clearly, overestimation of water saturation means underestimation of oil saturation and eventually, underestimation of the reserves. To demonstrate this impact further, for S-

group of networks, the differences are calculated between actual and estimated oil saturations ($\frac{\text{Actual } So\text{- Estimated } So}{\text{Actual } So} \times 100\%$) and are shown in the Fig. 4.25.

Chapter 5. Discussion & conclusion

We improved the model of Zolfaghari and Piri (2015a) to calculate the electrical properties of porous media during drainage and imbibition flow cycles. The model investigates the impact of microporosity on the electrical properties of porous media where the wetting phase resides at corners. To do so, we built angular pore networks on 2D lattices and added microporosity regions to generate bimodal pore networks. Five different groups of pore networks were generated to study the impact of variable arrangements of the microporosity regions. The results show that the intraparticle microporosity can significantly lower electrical resistance by providing a shorter pathway for the electrical current. Pro-vertical micro-networks (parallel microporosity) do not affect electrical properties as much since they do not alter the shortest path of the flow. In-series microporosity has a much more significant effect on the electrical properties. Electrical tortuosity has a strong positive correlation with the electrical resistance: higher tortuosity means higher electrical resistance. Using representative 3D pore networks, we also calculated the Resistivity Index (RI) of Estaillades limestone and Berea sandstone samples. We demonstrated the non-Archie behavior of RI at low water saturation in a more heterogeneous sample, i.e., Estaillades limestone. The fact of having a very wide range of pore sizes and the pore volume distributed irregularly throughout the network is the underlying cause of sudden changes in water saturation of Estaillades networks which can be observed on the RI curve with drastic changes of the original slope. Since the

majority of larger pores are surrounded by small pores, oil invades larger pores instantaneously once the neighboring smaller pores are invaded during drainage. Therefore, a large volume of water is displaced in a single displacement event causing an abrupt change in the water saturation. Further work needs to be done to incorporate Archie parameters such as saturation exponent and cementation factor in the Pore Network Models.

We also simulated microporosity regions of a reservoir carbonate sample using our developed Pore-Scale Network Model. We specifically studied the effect of different local porosities and pore size distributions of microporosity zones by generating stochastic pore networks within the Euclidean space of the microporosity clusters.

Results indicate that pore size distribution within the microporosity zone has a much stronger impact on the results (i.e., capillary pressure, relative permeabilities and resistivity index curve) rather than local porosity. However, as the micropore sizes are increasing, results vary in a wide range and show more sensitivity to the local porosity values. Generally, the pore networks generated with the chosen small Pore Size Distribution (PSD) of the micropores seems to better replicate the pore space in microporosity zone. Resistivity Index curve for this group of networks shows non-Archie behavior with two slopes which is consistent with the simulated result of Estaillades limestone.

References

Aghaei, A. & Piri, M. (2015). Direct pore-to-core up-scaling of displacement processes: Dynamic pore network modeling and experimentation. Journal of hydrology, 522, 488-509.

Ahmed, T. (2010). Reservoir engineering Handbook Gulf Professional Publishing.

Ahr, W. M. (2011). Geology of carbonate reservoirs: the identification, description and characterization of hydrocarbon reservoirs in carbonate rocks. John Wiley & Sons.

Ahrenholz, B., Tölke, J., Lehmann, P., Peters, A., Kaestner, A., Krafczyk, M., & Durner, W. (2008). Prediction of capillary hysteresis in a porous material using lattice-Boltzmann methods and comparison to experimental data and a morphological pore network model. Advances in Water Resources, 31(9), 1151-1173.

Akbar, M., Vissapragada, B., Alghamdi, A. H., Allen, D., Herron, M., Carnegie, A., Dutta, D., Olesen, J.R., Chourasiya, R.D., Logan, D. & Stief, D. (2000). A snapshot of carbonate reservoir evaluation. Oilfield Review, 12(4), 20-21.

Al-Marzouqi, M. I., Budebes, S., Sultan, E., Bush, I., Griffiths, R., Gzara, K. B., ... & Montaron, B. (2010). Resolving carbonate complexity. Oilfield review, 22(2), 40-55.

Archie, G. E. (1942). The electrical resistivity log as an aid in determining some reservoir characteristics. Transactions of the AIME, 146(01), 54-62.

Bauer, D., Youssef, S., Fleury, M., Bekri, S., Rosenberg, E., & Vizika, O. (2012). Improving the estimations of petrophysical transport behavior of carbonate rocks using a dual pore network approach combined with computed microtomography. Transport in porous media, 94(2), 505-524.

Bauer, D., Youssef, S., Han, M., Bekri, S., Rosenberg, E., Fleury, M., & Vizika, O. (2011). From computed microtomography images to resistivity index calculations of heterogeneous carbonates using a dual-porosity pore-network approach: Influence of percolation on the electrical transport properties. Physical review E, 84(1), 011133.

Bear, J., Tsang, C. F., & De Marsily, G. (2012). Flow and contaminant transport in fractured rock. Academic Press.

Bekri, S., Laroche, C., & Vizika, O. (2005, August). Pore network models to calculate transport and electrical properties of single or dual-porosity rocks. In SCA (Vol. 35, p. 2005).

Blunt, M. J. (2017). Multiphase flow in permeable media: A pore-scale perspective. Cambridge University Press.

Blunt, M. J., Bijeljic, B., Dong, H., Gharbi, O., Iglauer, S., Mostaghimi, P., Paluszny, A. & Pentland, C. (2013). Pore-scale imaging and modelling. Advances in Water Resources, 51, 197-216.

Blunt, M. J., Jackson, M. D., Piri, M., & Valvatne, P. H. (2002). Detailed physics, predictive capabilities and macroscopic consequences for pore-network models of multiphase flow. Advances in Water Resources, 25(8-12), 1069-1089.

Boek, E. S., & Venturoli, M. (2010). Lattice-Boltzmann studies of fluid flow in porous media with realistic rock geometries. Computers & Mathematics with Applications, 59(7), 2305-2314.

Boyd, A., Darling, H., Tabanou, J., Davis, B., Lyon, B., Flaum, C., Klein J., Sneider R., Sibbit A. & Singer, J. (1995). The lowdown on low-resistivity pay. Oilfield Review, 7(3), 4-18.

Bultreys, T., De Boever, W., & Cnudde, V. (2016). Imaging and image-based fluid transport modeling at the pore scale in geological materials: A practical introduction to the current state-of-the-art. Earth-Science Reviews, 155, 93-128.

Bultreys, T., Lin, Q., Gao, Y., Raeini, A. Q., AlRatrout, A., Bijeljic, B., & Blunt, M. J. (2018). Validation of model predictions of pore-scale fluid distributions during two-phase flow. Physical Review E, 97(5), 053104.

Bultreys, T., Van Hoorebeke, L., & Cnudde, V. (2015). Multi-scale, micro-computed tomography-based pore network models to simulate drainage in heterogeneous rocks. Advances in Water Resources, 78, 36-49.

Cantrell, D. L., & Hagerty, R. M. (1999). Microporosity in arab formation carbonates, Saudi Arabia. GeoArabia, 4(2), 129-154.

Chin, J. (2002). Lattice Boltzmann simulation of the flow of binary immiscible fluids with different viscosities using the Shan-Chen microscopic interaction model. Philosophical Transactions of the Royal Society of London. Series A: Mathematical, Physical and Engineering Sciences, 360(1792), 547-558.

Choquette, P. W., & Pray, L. C. (1970). Geologic nomenclature and classification of porosity in sedimentary carbonates. AAPG bulletin, 54(2), 207-250.

Clennell, M. B. (1997). Tortuosity: a guide through the maze. Geological Society, London, Special Publications, 122(1), 299-344.

Coates, G. R., Xiao, L., & Prammer, M. G. (1999). NMR logging: principles and applications (Vol. 234). Houston: Haliburton Energy Services.

Doveton, J. H. (2001). Development of an Archie Equation Model for Log Analysis of Pennsylvanian Oomoldic Zones in Kansas. KGS Open File Report.

Ehrenberg, S. N., & Walderhaug, O. (2015). Preferential calcite cementation of macropores in microporous limestones. Journal of Sedimentary Research, 85(7), 780-793.

Fatt, I. (1956). The network model of porous media.

Fleury, M., Efnik, M., & Kalam, M. Z. (2004, October). Evaluation of water saturation from resistivity in a carbonate field. From laboratory to logs. In Proceedings of International Symposium of the Society of Core Analysts, Abu Dhabi, UAE (pp. 5-9).

Gundogar, A. S., Ross, C. M., Akin, S., & Kovscek, A. R. (2016). Multiscale pore structure characterization of Middle East carbonates. Journal of Petroleum Science and Engineering, 146, 570-583.

Hakimov, N., Zolfaghari, A., Kalantari-Dahaghi, A., Negahban, S., & Gunter, G. (2018, November). Pore-Scale Network Modeling of Petrophysical Properties in Samples with Wide Pore Size Distributions. In Abu Dhabi International Petroleum Exhibition & Conference. Society of Petroleum Engineers.

Hamada, G. M., Almajed, A. A., Okasha, T. M., & Algathe, A. A. (2013). Uncertainty analysis of Archie's parameters determination techniques in carbonate reservoirs. Journal of Petroleum Exploration and Production Technology, 3(1), 1-10.

Hassan, A., Chandra, V., Yutkin, M. P., Patzek, T. W., & Espinoza, D. N. (2019). Imaging and Characterization of Microporous Carbonates Using Confocal and Electron Microscopy of Epoxy Pore Casts. SPE Journal.

Icardi, M., Boccardo, G., Marchisio, D. L., Tosco, T., & Sethi, R. (2014). Pore-scale simulation of fluid flow and solute dispersion in three-dimensional porous media. Physical review E, 90(1), 013032.

Jiang, Z., Van Dijke, M. I. J., Sorbie, K. S., & Couples, G. D. (2013). Representation of multiscale heterogeneity via multiscale pore networks. Water resources research, 49(9), 5437-5449.

Jiang, Z., Van Dijke, M. I. J., Wu, K., Couples, G. D., Sorbie, K. S., & Ma, J. (2012). Stochastic pore network generation from 3D rock images. Transport in porous media, 94(2), 571-593.

Joekar-Niasar, V., Hassanizadeh, S. M., & Dahle, H. K. (2010). Non-equilibrium effects in capillarity and interfacial area in two-phase flow: dynamic pore-network modelling. Journal of Fluid Mechanics, 655, 38-71.

Karpyn, Z. T., & Piri, M. (2007). Prediction of fluid occupancy in fractures using network modeling and x-ray microtomography. I: Data conditioning and model description. Physical Review E, 76(1), 016315.

Leon y Leon, C. A. L. (1998). New perspectives in mercury porosimetry. Advances in colloid and interface science, 76, 341-372.

Mayer, R. P., & Stowe, R. A. (1965). Mercury porosimetry—breakthrough pressure for penetration between packed spheres. Journal of colloid Science, 20(8), 893-911.

Meakin, P., & Tartakovsky, A. M. (2009). Modeling and simulation of pore-scale multiphase fluid flow and reactive transport in fractured and porous media. Reviews of Geophysics, 47(3).

Mehmani, A., & Prodanović, M. (2014). The effect of microporosity on transport properties in porous media. Advances in Water Resources, 63, 104-119.

Miao, X., Gerke, K. M., & Sizonenko, T. O. (2017). A new way to parameterize hydraulic conductances of pore elements: A step towards creating pore-networks without pore shape simplifications. Advances in water resources, 105, 162-172.

Mohammadmoradi, P., & Kantzas, A. (2017). Toward direct pore-scale modeling of three-phase displacements. Advances in water resources, 110, 120-135.

Morad, D., Paganoni, M., Al Harthi, A., Morad, S., Ceriani, A., Mansurbeg, H., Al Suwaidi, A., Al-Aasm, I.S & Ehrenberg, S. N. (2018). Origin and evolution of microporosity in packstones and grainstones in a Lower Cretaceous carbonate reservoir, United Arab Emirates. Geological Society, London, Special Publications, 435(1), 47-66.

Norbisrath, J. H., Eberli, G. P., Laurich, B., Desbois, G., Weger, R. J., & Urai, J. L. (2015). Electrical and fluid flow properties of carbonate microporosity types from multiscale digital image analysis and mercury injection. AAPG Bulletin, 99(11), 2077-2098.

Oren, P. E., Bakke, S., & Arntzen, O. J. (1997, January). Extending predictive capabilities to network models. In SPE Annual Technical Conference and Exhibition. Society of Petroleum Engineers.

Pak, T., Butler, I. B., Geiger, S., van Dijke, M. I., Jiang, Z., & Surmas, R. (2016). Multiscale pore-network representation of heterogeneous carbonate rocks. Water Resources Research, 52(7), 5433-5441.

Pan, C., Hilpert, M., & Miller, C. T. (2004). Lattice-Boltzmann simulation of two-phase flow in porous media. Water Resources Research, 40(1).

Piri, M. (2003). "Pore-scale modelling of three-phase flow." *PhD Disseration. Imperial College*.

Piri, M., & Blunt, M. J. (2005a). Three-dimensional mixed-wet random pore-scale network modeling of two-and three-phase flow in porous media. I. Model description. Physical Review E, 71(2), 026301.

Piri, M., & Blunt, M. J. (2005b). Three-dimensional mixed-wet random pore-scale network modeling of two-and three-phase flow in porous media. II. Results. Physical Review E, 71(2), 026302.

Piri, M., & Karpyn, Z. T. (2007). Prediction of fluid occupancy in fractures using network modeling and X-ray microtomography. II: Results. Physical Review E, 76(1), 016316.

Princen, H. M. (1969a). Capillary phenomena in assemblies of parallel cylinders: I. Capillary rise between two cylinders. Journal of Colloid and Interface Science, 30(1), 69-75.

Princen, H. M. (1969b). Capillary phenomena in assemblies of parallel cylinders: II. Capillary rise in systems with more than two cylinders. Journal of Colloid and Interface Science, 30(3), 359-371.

Princen, H. M. (1970). Capillary phenomena in assemblies of parallel cylinders: III. Liquid columns between horizontal parallel cylinders. Journal of Colloid and Interface Science, 34(2), 171-184.

Prodanović, M., Mehmani, A., & Sheppard, A. P. (2015). Imaged-based multiscale network modelling of microporosity in carbonates. Geological Society, London, Special Publications, 406(1), 95-113.

Raeini, A. Q., Bijeljic, B., & Blunt, M. J. (2015). Modelling capillary trapping using finite-volume simulation of two-phase flow directly on micro-CT images. Advances in Water Resources, 83, 102-110.

Rahman, M. H., Pierson, B. J., Yusoff, W., & Ismail, W. (2011, January). Classification of microporosity in carbonates: examples from miocene carbonate reservoirs of central luconia, offshore sarawak, malaysia. In International petroleum technology conference. International Petroleum Technology Conference.

Ramstad, T., Idowu, N., Nardi, C., & Øren, P. E. (2012). Relative permeability calculations from two-phase flow simulations directly on digital images of porous rocks. Transport in Porous Media, 94(2), 487-504.

Ramstad, T., Øren, P. E., & Bakke, S. (2010). Simulation of two-phase flow in reservoir rocks using a lattice Boltzmann method. Spe Journal, 15(04), 917-927.

Ruspini, L. C., Farokhpoor, R., & Øren, P. E. (2017). Pore-scale modeling of capillary trapping in water-wet porous media: A new cooperative pore-body filling model. Advances in Water Resources, 108, 1-14.

Satter, A., & Iqbal, G. M. (2015). Reservoir Engineering: The fundamentals, simulation, and management of conventional and unconventional recoveries. Gulf Professional Publishing.

Sheng, J. (Ed.). (2013). Enhanced oil recovery field case studies. Gulf Professional Publishing.

Sheng, Q., & Thompson, K. (2013). Dynamic coupling of pore-scale and reservoir-scale models for multiphase flow. Water Resources Research, 49(9), 5973-5988.

Soulaine, C., Gjetvaj, F., Garing, C., Roman, S., Russian, A., Gouze, P., & Tchelepi, H. A. (2016). The impact of sub-resolution porosity of X-ray microtomography images on the permeability. Transport in Porous Media, 113(1), 227-243.

Swanson, B. F. (1985). Microporosity in reservoir rocks: Its measurement and influence on electrical resistivity. The Log Analyst, 26(06).

Talabani, S., Boyd, D., El Wazeer, F., & Al Arfi, S. (2000, January). Validity of Archie equation in carbonate rocks. In Abu Dhabi International Petroleum Exhibition and Conference. Society of Petroleum Engineers.

Thommes, M., Smarsly, B., Groenewolt, M., Ravikovitch, P. I., & Neimark, A. V. (2006). Adsorption hysteresis of nitrogen and argon in pore networks and characterization of novel micro-and mesoporous silicas. Langmuir, 22(2), 756-764.

Vogel, H. J., Tölke, J., Schulz, V. P., Krafczyk, M., & Roth, K. (2005). Comparison of a lattice-Boltzmann model, a full-morphology model, and a pore network model for determining capillary pressure–saturation relationships. Vadose Zone Journal, 4(2), 380-388.

Xiong, Q., Baychev, T. G., & Jivkov, A. P. (2016). Review of pore network modelling of porous media: experimental characterisations, network constructions and applications to reactive transport. Journal of contaminant hydrology, 192, 101-117.

Yang, J., Bondino, I., Regaieg, M., & Moncorgé, A. (2017). Pore to pore validation of pore network modelling against micromodel experiment results. Computational Geosciences, 21(5-6), 849-862.

Zolfaghari, A. (2014). "Pore-scale Network Modeling of Two-and Three-phase Flow Based on Thermodynamically Consistent Threshold Capillary Pressures" *PhD Disseration. University of Wyoming*.

Zolfaghari, A., & Piri, M. (2017a). Pore-scale network modeling of three-phase flow based on thermodynamically consistent threshold capillary pressures. I. Cusp formation and collapse. Transport in porous media, 116(3), 1093-1137.

Zolfaghari, A., & Piri, M. (2017b). Pore-scale network modeling of three-phase flow based on thermodynamically consistent threshold capillary pressures. II. Results. Transport in Porous Media, 116(3), 1139-1165.

Appendices

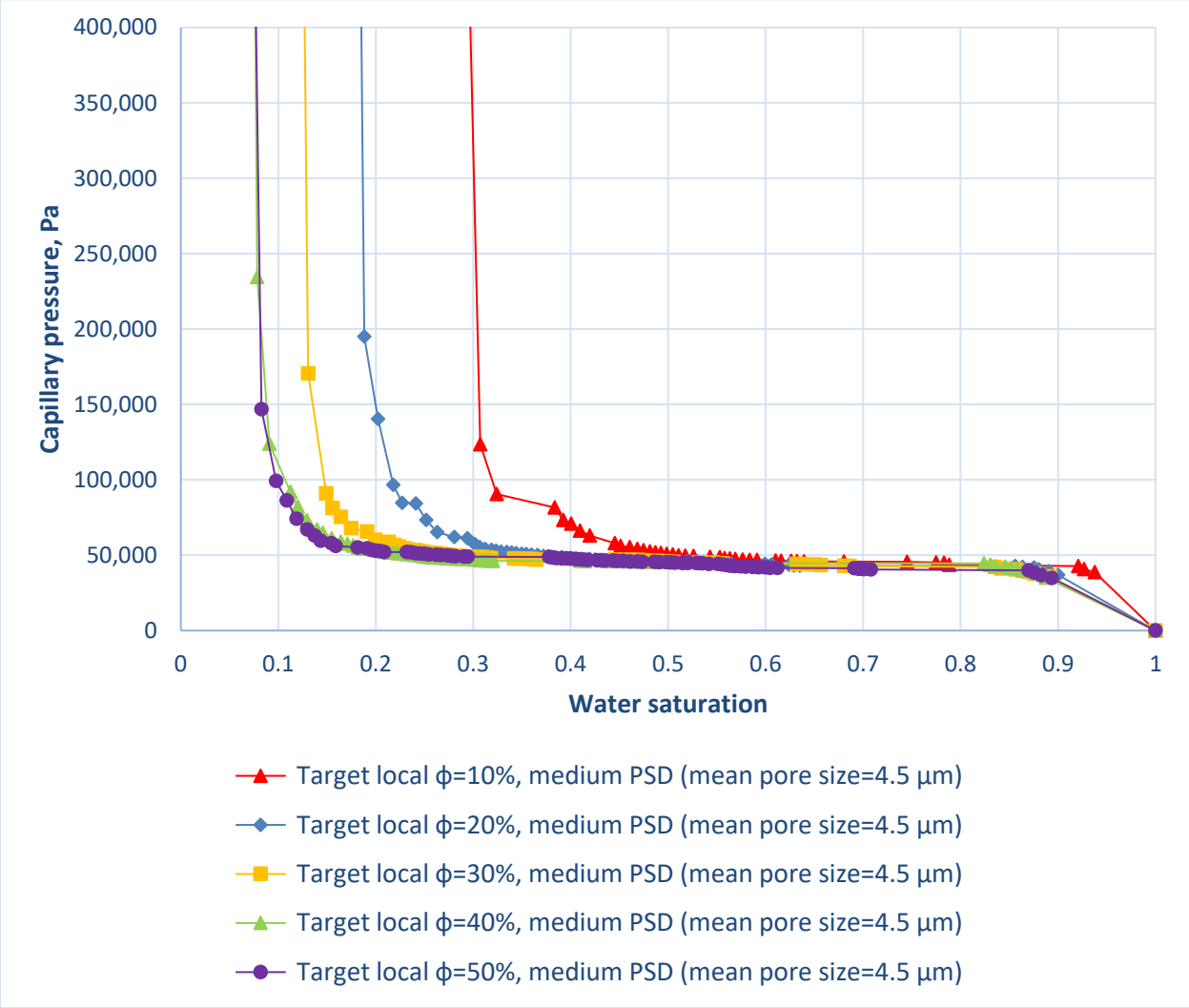

Figure A-1. Capillary pressure curves during primary drainage generated for the pore-networks with the medium-sized micro pores in microporosity zones.

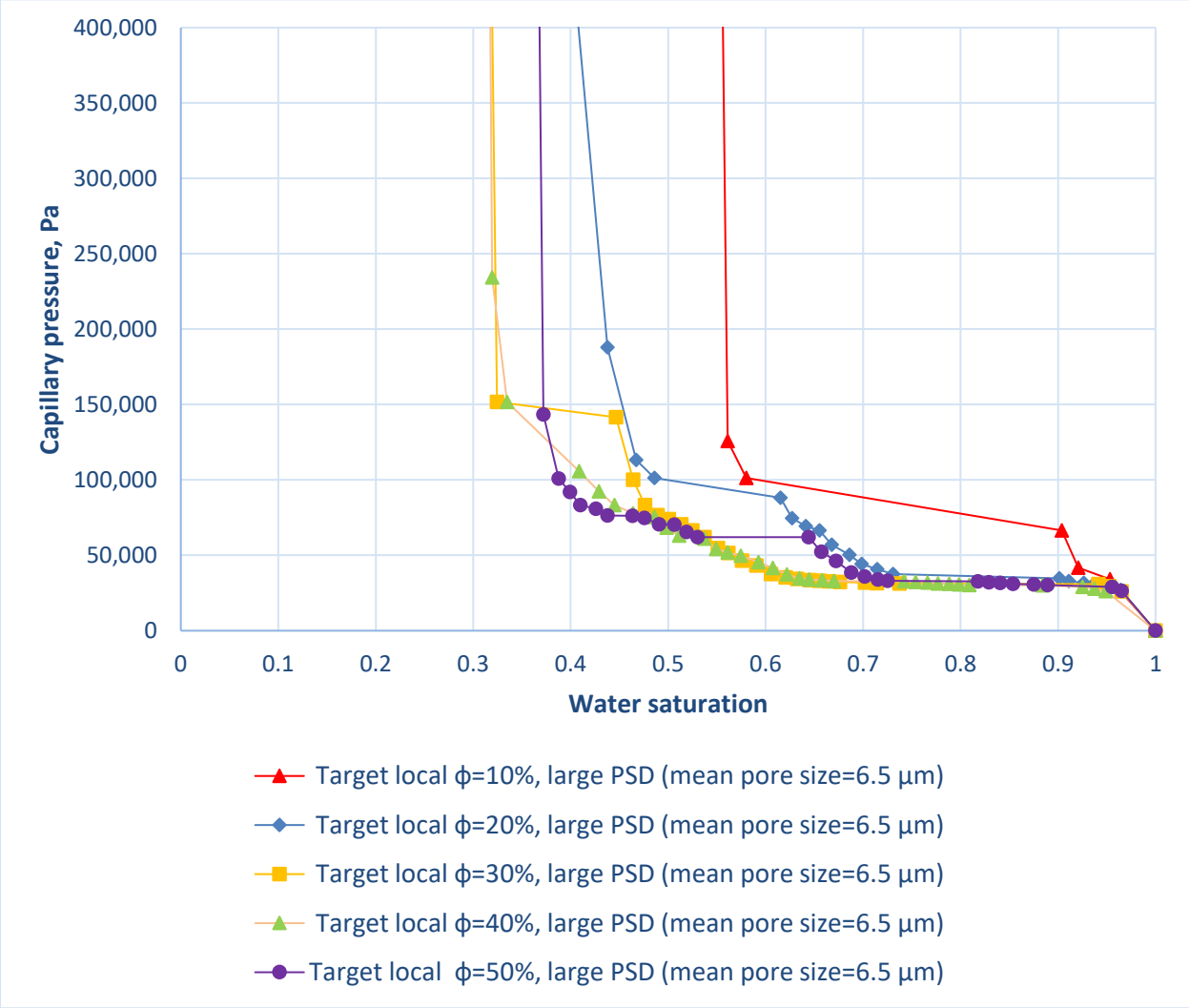

Figure A-2. Capillary pressure curves during primary drainage generated for the pore-networks with the large-sized micro pores in microporosity zones.

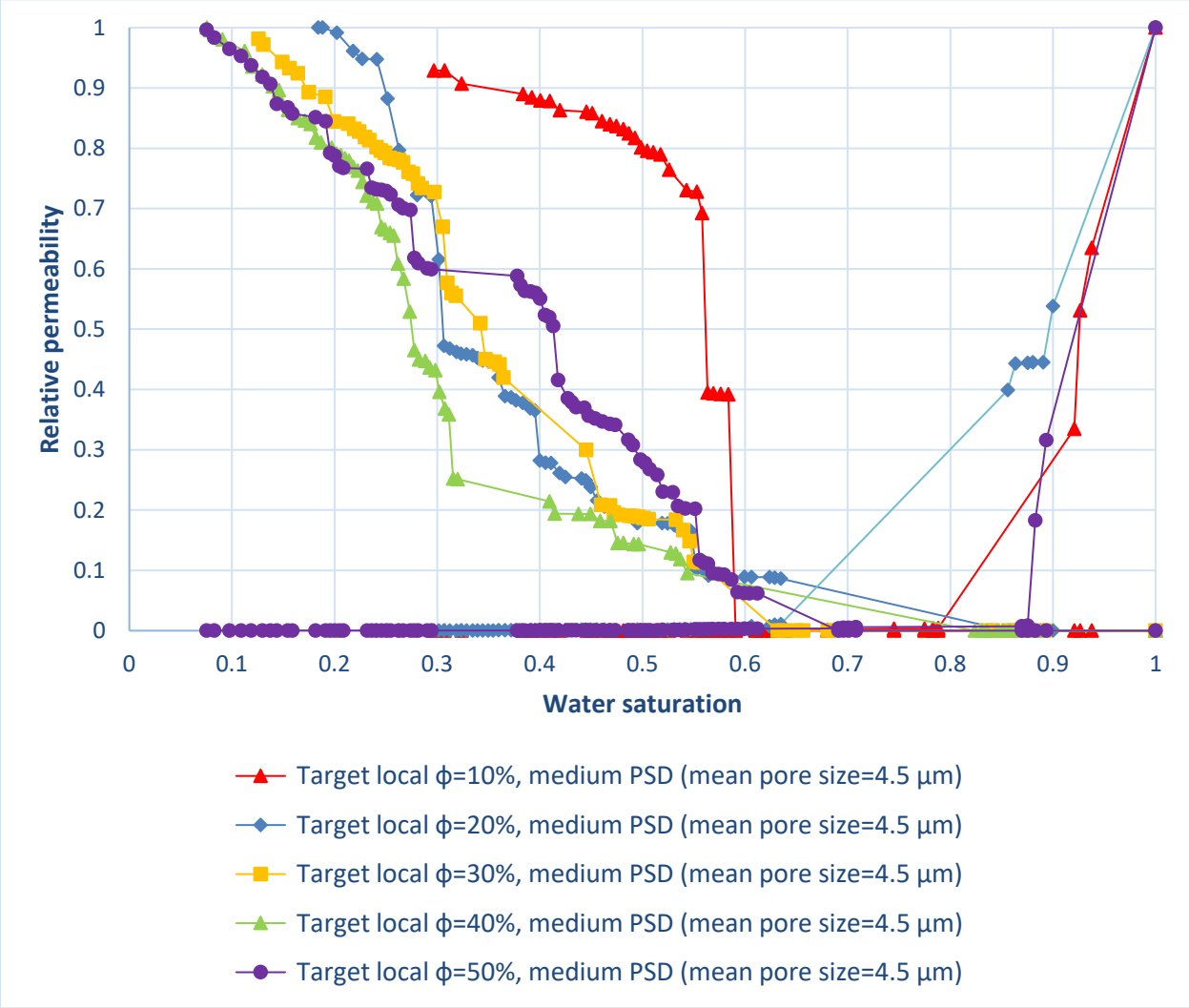

Figure A-3. Relative permeability curves during primary drainage generated for the pore-networks with the medium-sized micro pores in microporosity zones.

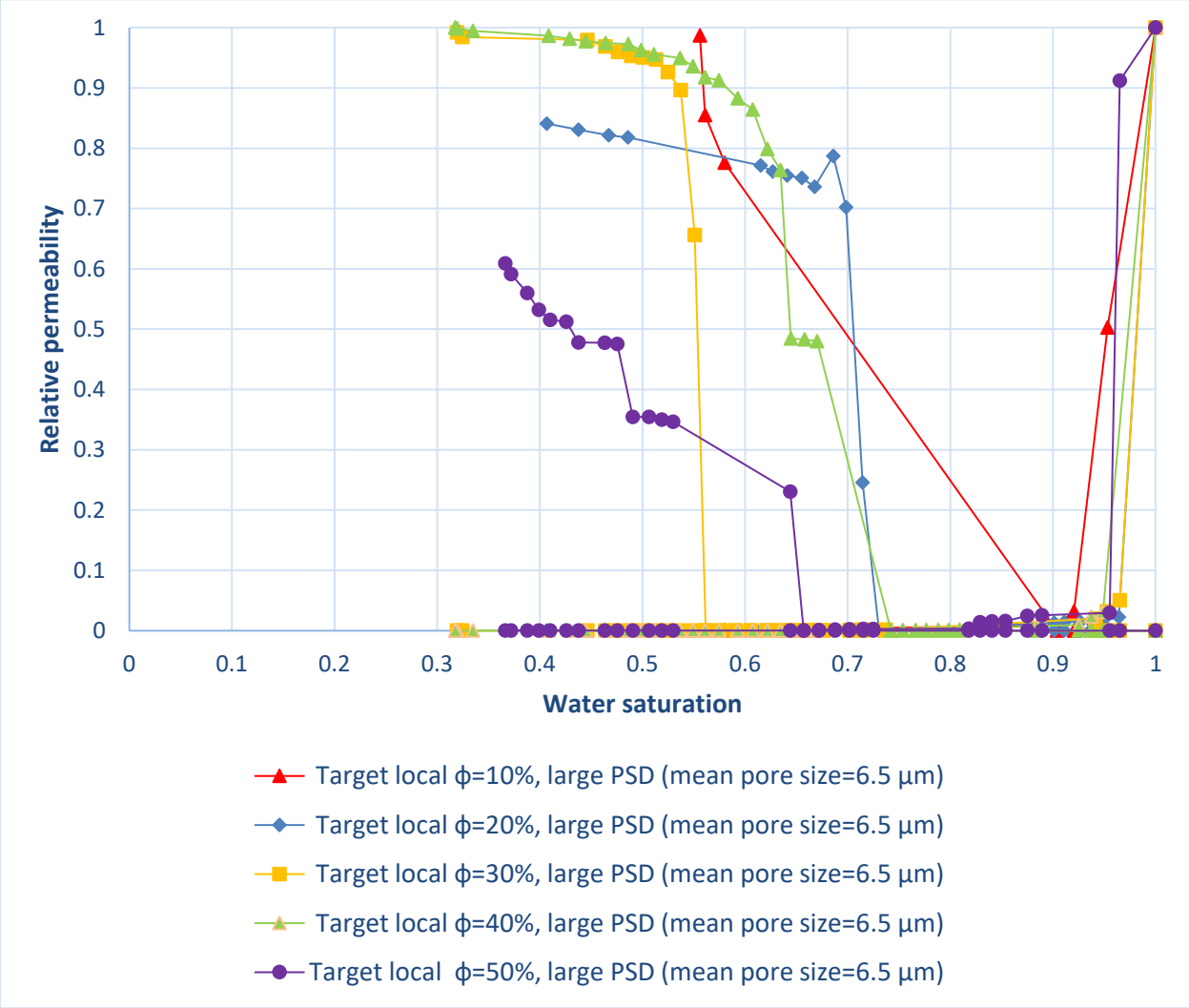

Figure A-4. Relative permeability curves during primary drainage generated for the pore-networks with the large-sized micro pores in microporosity zones.

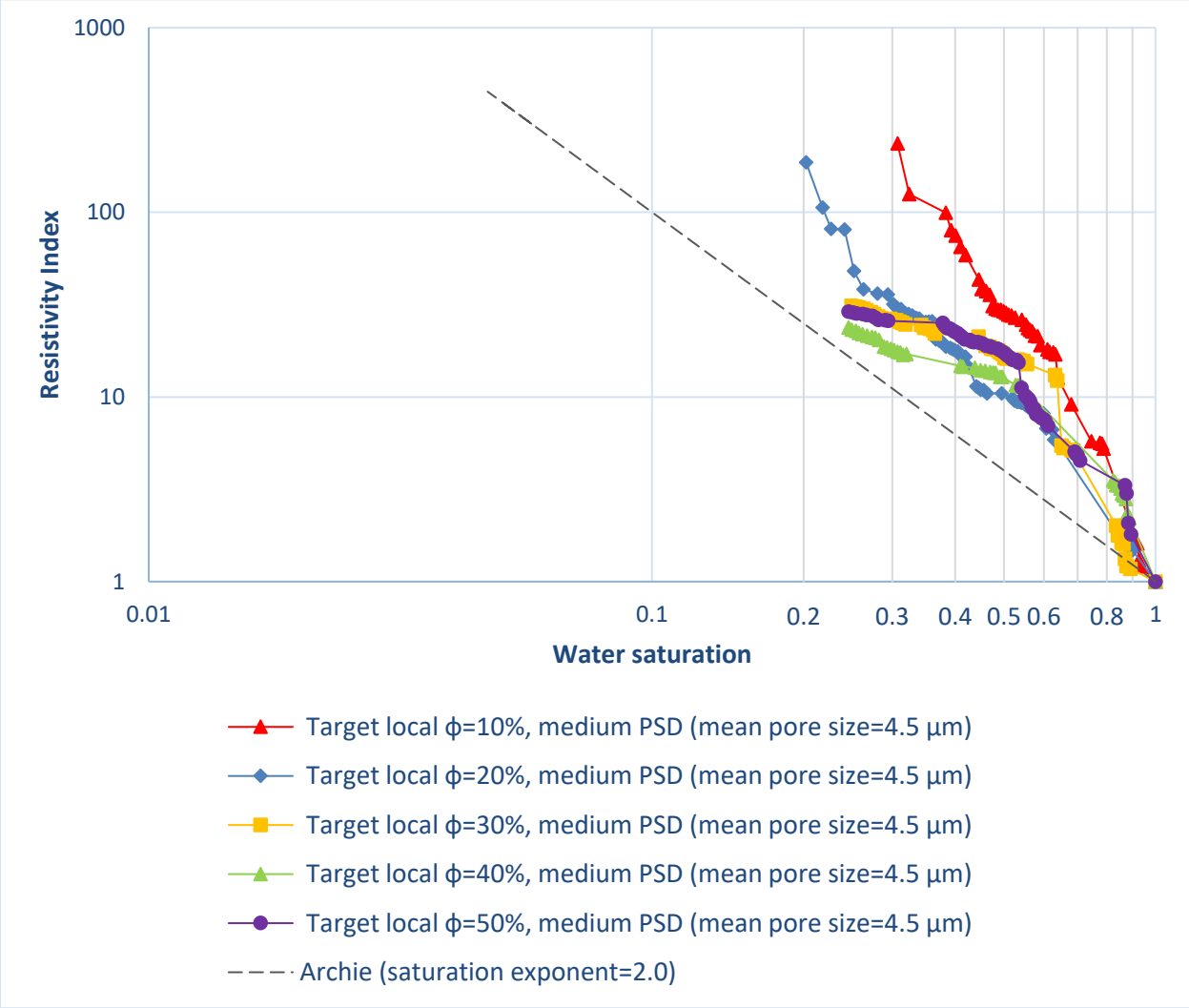

Figure A-5. Resistivity Index curves during primary drainage generated for the pore-networks with the medium-sized micro pores in microporosity zones. Both axes are shown in log-scale.

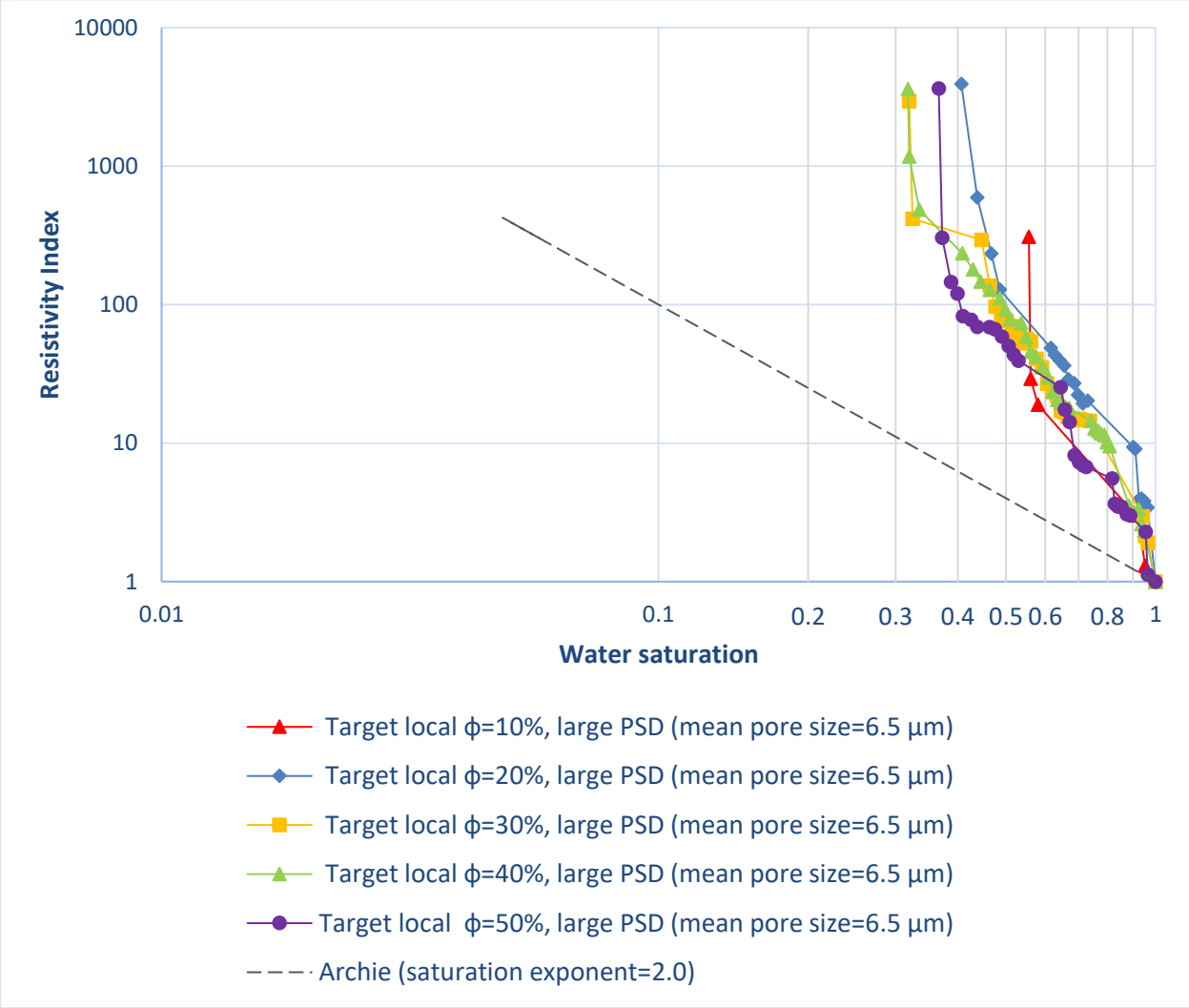

Figure A-6. Resistivity Index curves during primary drainage generated for the pore-networks with the large-sized micro pores in microporosity zones. Both axes are shown in log-scale.

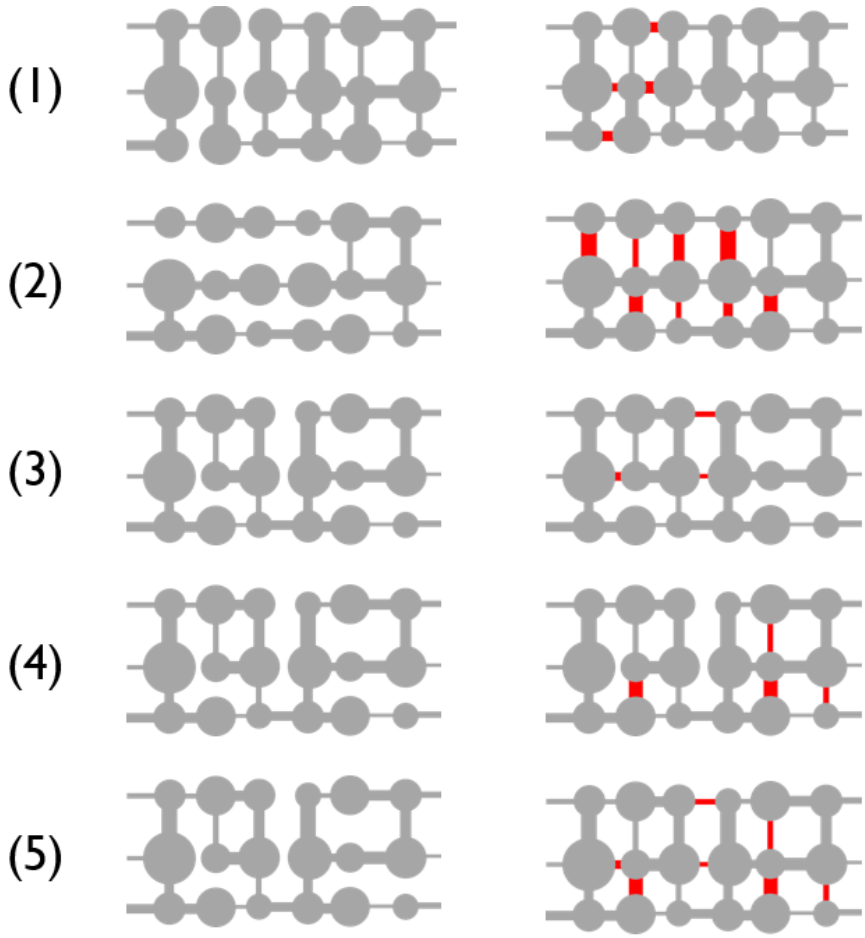

Figure A-7. Five different groups of 2D pore networks with their included microporosity regions. Base pore networks are shown on the left. Same pore networks with the inserted micro-networks in red are shown on the right (Hakimov et al. 2018). Reprinted by permission of Copyright SPE.

			Tortuosity	
	Pore-network	microPV/totalPV	Electrical	Flow
GROUP 1	A1-base PN	0.00%	4.54	4.528
	B	1.67%	3.509	3.518
	C	3.97%	1.928	1.991
	D	7.26%	1.634	1.682
	E	8.32%	1.402	1.374
GROUP 2	A2-base PN	0.00%	1.091	1.091
	B	0.49%	1.116	1.099
	C	1.37%	1.156	1.101
	D	2.17%	1.172	1.101
GROUP 3	A3-base PN	0.00%	1.489	1.42
	B	0.88%	1.328	1.385
	C	1.37%	1.263	1.31
	D	2.43%	1.225	1.228
GROUP 4	A3-base PN	0.00%	1.498	1.522
	B	0.60%	1.588	1.632
	C	1.21%	1.632	1.678
	D	1.75%	1.65	1.711
GROUP 5	A3-base PN	0.00%	1.501	1.545
	B	1.77%	1.43	1.548
	C	2.93%	1.406	1.456
	D	4.13%	1.38	1.392

Figure A-8. The percentages of microporosity regions and the electrical and flow tortuosities in all pore networks generated in this work (Hakimov et al. 2018). Reprinted by permission of Copyright SPE.

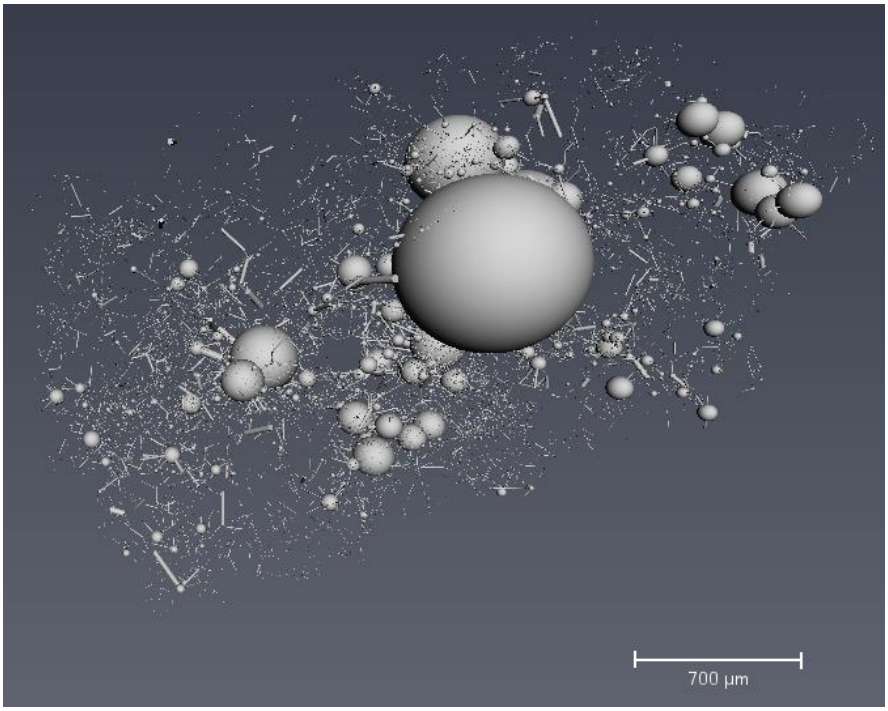

Figure A-9. Pore Network of the Estaillades-2 sub-volume where both pores and throats are shown.